Antarctic Thermocline Dynamics along a Narrow Shelf with Easterly Winds

Tore Hattermann

Alfred Wegener Institute, Bremerhaven, Germany, and Akvaplan-niva AS, Tromsø, Norway

(Manuscript received 3 April 2018, in final form 28 August 2018)

ABSTRACT

Determining the role of Southern Ocean warm intermediate water for driving melting of the Antarctic ice sheet is a major challenge in assessing future sea level rise. Analysis of 2859 CTD profiles obtained between 1977 and 2016 by ships and instrumented seals at the Weddell Sea continental slope reveals a seasonal rise of the Antarctic Slope Front thermocline by more than 100 m during the summer. The signal at Kapp Norvegia (17°W) corresponds with a seasonal warming downstream at the Filchner Trough (40°W), indicating that a coherent evolution of the slope front along the shelf break regulates the onshore flow of warm deep water. Climatological cross sections of the slope front hydrography show that downwelling of Antarctic Surface Water forms a secondary front above the warm deep water interface during summer. Enhanced baroclinic growth rates at this front suggest that the wind-driven suppression of the thermocline is partially compensated by a shallower eddy overturning cell when surface water is present. A simple model of the Weddell Gyre boundary current reveals that wintertime densification of surface waters is crucial for maintaining the deep thermocline along the eastern Weddell Sea coast. The sensitivity of the warm inflow to the cross-frontal density gradient implies a positive feedback with ice shelf melting that may lead to an abrupt transition into a high melting state once warm water rises over the shelf break depth. Despite its regional focus, this study highlights the role of upper ocean buoyancy fluxes for controlling the thermocline depth along seasonally ice-covered narrow shelf regions with cyclonic along-slope winds.

1. Introduction

The Weddell Gyre plays an important role in the climate system by advecting heat toward the Antarctic ice shelves (Nicholls et al. 2009) and by feeding Antarctic Bottom Water into the global ocean overturning circulation (Jullion et al. 2014; Orsi et al. 2002). Comparatively warm and saline warm deep water (WDW) that derives from the voluminous midlayer Circumpolar Deep Water of the Antarctic Circumpolar Current enters the gyre at around 30°E (Ryan et al. 2016) and merges with the Antarctic Slope Current,[1] which circulates anticlockwise around the continent (Peña-Molino et al. 2016; Heywood et al. 1998). Unlike in West Antarctica, where inflow of Circumpolar Deep water to the continental shelf drives Antarctic ice loss (Pritchard et al. 2012) and fresh meltwater input (Naveira Garabato et al. 2017), ocean temperatures on the Weddell Sea continental shelf are presently close to the surface freezing point year-round (Nicholls et al. 2009). In particular along the narrow eastern Weddell Sea shelf (from 30°E to 20°W), downwelling due to steady easterly winds suppresses the WDW thermocline below the depth of the shelf break, maintaining the Antarctic Slope Front (ASF), thereby protecting the glaciated coast from intrusion of warmer water (Sverdrup 1953; Ohshima et al. 1996).

At the same time, changes of the Weddell Gyre dynamics are being observed that require a better understanding of processes at play. Deep water masses in the eastern Weddell Sea have warmed on decadal time scales (Couldrey et al. 2013; Smedsrud 2005), while Antarctic surface waters have been freshening since the 1960s (de Lavergne et al. 2014). Strengthening of the subpolar westerlies (Thompson and Solomon 2002) causes stronger upwelling of carbon- and nutrient-rich deep water (Hoppema et al. 2015). Sea ice extent in the

---

[1] Here the term "slope current" also refers to the Antarctic Coastal Current, which is merged with the Weddell Gyre boundary current along the eastern Weddell Sea coast, but separates from the slope current in regions where the continental shelf widens around Antarctica (Heywood et al. 2004).

ᵃ Denotes content that is immediately available upon publication as open access.

Corresponding author: Tore Hattermann, tore.hattermann@awi.de, tore.hattermann@npolar.no

Weddell Sea has declined slightly during winter but strongly increased during the summer (Parkinson and Cavalieri 2012). Intermittent intrusions of warmer water onto the shelf have recently been observed (Darelius et al. 2016; Hattermann et al. 2012), and models suggest that a rise of the WDW above the shelf break may trigger a regime shift toward significantly increased mass loss in this sector of Antarctica (Hellmer et al. 2012, 2017; Timmermann and Goeller 2017). Expected changes for the coming century also include decline in sea ice (Naughten et al. 2018), concurrent upper ocean freshening (Bernardello et al. 2014), a shoaling of the upper mixed layer (Salleé et al. 2013), and increased ice shelf basal melting due to surface warming along the eastern Weddell Sea coast (Kusahara and Hasumi 2013).

Although it is generally acknowledged that the ASF plays a crucial role for ice-shelf stability, sea ice production, and dense water formation, the quantification of the processes that control the transport of WDW across the front and their possible responses to climate change carries large uncertainties. The relevant physical processes that maintain temperature gradients of several centigrade over less than 100-km horizontal distance across the front involve various processes that are not well captured by large-scale and climate simulations, such as waves and hydrographic anomalies along the shelf break (Graham et al. 2013; Chavanne et al. 2010), local atmospheric forcing on stratification and circulation on the shelf (Petty et al. 2013; Darelius et al. 2016), or interaction with local bathymetry (St-Laurent et al. 2013) and adjacent ice shelves (Price et al. 2008; Langley et al. 2014).

Recent observations and high-resolution modeling suggest an important role of mesoscale eddies in regulating onshore transports of WDW (Nøst et al. 2011; Thompson et al. 2014). Formed by instabilities in the slope current, these eddies counteract the wind-driven downwelling and eventually determine the WDW thermocline depth along the shelf break (Hattermann et al. 2014). However, the dynamical drivers and the variability of this eddy-compensated overturning circulation, which is particularly important in the boundary region of the gyre (Su et al. 2014), are not fully understood. In particular, the transient response of cross-frontal transport to the pronounced seasonality of sea ice and atmospheric forcing is difficult to assess. The strength of the slope current generally follows the large-scale wind forcing (Nuñez-Riboni and Fahrbach 2009) and observations show that traces of WDW access the continental shelf usually during summer (Årthun et al. 2012; Ryan et al. 2017). Models suggest that the depth of the WDW thermocline and eddy transports are sensitive to changes in easterly wind stress (Stewart and Thompson 2015; Hattermann et al. 2014) but also respond to surface buoyancy forcing, which is mainly determined

by the annual cycle of freezing and melting of sea ice (Zhou et al. 2014; Stewart and Thompson 2016; Daae et al. 2017).

The objectives of this study are 1) to provide a better understanding of the spatial structure and seasonality of the slope front from available hydrographic observations and 2) to gain insights into the driving mechanisms of thermocline excursions (on seasonal and longer time scales) that control the availability of warm water for glacial melting and possible responses to future changes. The analysis is focused around Kapp Norvegia, approximately at 17°W, where coherent observations of the slope front are available and a relatively undisturbed shelf break topography allows regional averaging. The region comprises the Weddell Gyre boundary current as it follows the narrow eastern Weddell Sea continental shelf (Fig. 1). It also represents upstream conditions of the slope current and WDW thermocline that enter the wide continental shelf in the southern Weddell Sea, where it interacts with the Filchner–Ronne Ice Shelf.

The first objective is partially motivated by the need for realistic boundary conditions to force regional model simulations that are currently being developed. Current large-scale models are still too coarse to properly resolve the slope front structure and eddy dynamics at play, which requires horizontal resolution of $\mathcal{O}(1)\,\mathrm{km}$ (St-Laurent et al. 2013; Stewart and Thompson 2015). In addition, available ship-based observations are unable to capture the seasonal variability of the front because of the large summer bias (Jullion et al. 2014). Thus, to augment the temporal and spatial coverage of the historical ship-based data, hydrographic profiles from instrumented seals were employed that cover most of the winter months and provide unique insights into seasonal variability and processes around the Antarctic coast (e.g., Årthun et al. 2012; Fedak 2004; Pellichero et al. 2017). A total of 2859 temperature and salinity profiles were combined in this study to map the location of the WDW thermocline at the shelf break and investigate seasonal evolution of the slope front stability. Together with the analysis, a set of monthly climatological sections of hydrographic properties across the ASF is provided that is suitable for model forcing or validation (Hattermann and Rohardt 2018).

The second objective focuses on the effects of wind forcing and surface buoyancy fluxes on the slope front momentum balance and WDW thermocline depth. Previous studies argued that the wind-driven onshore Ekman transport and accumulation of sea ice meltwater from a larger area is the primary reason for maintaining the low salinities that are observed on the continental shelf in this region (Nøst et al. 2011; Zhou et al. 2014). General circulation models show that eddy kinetic energy of the
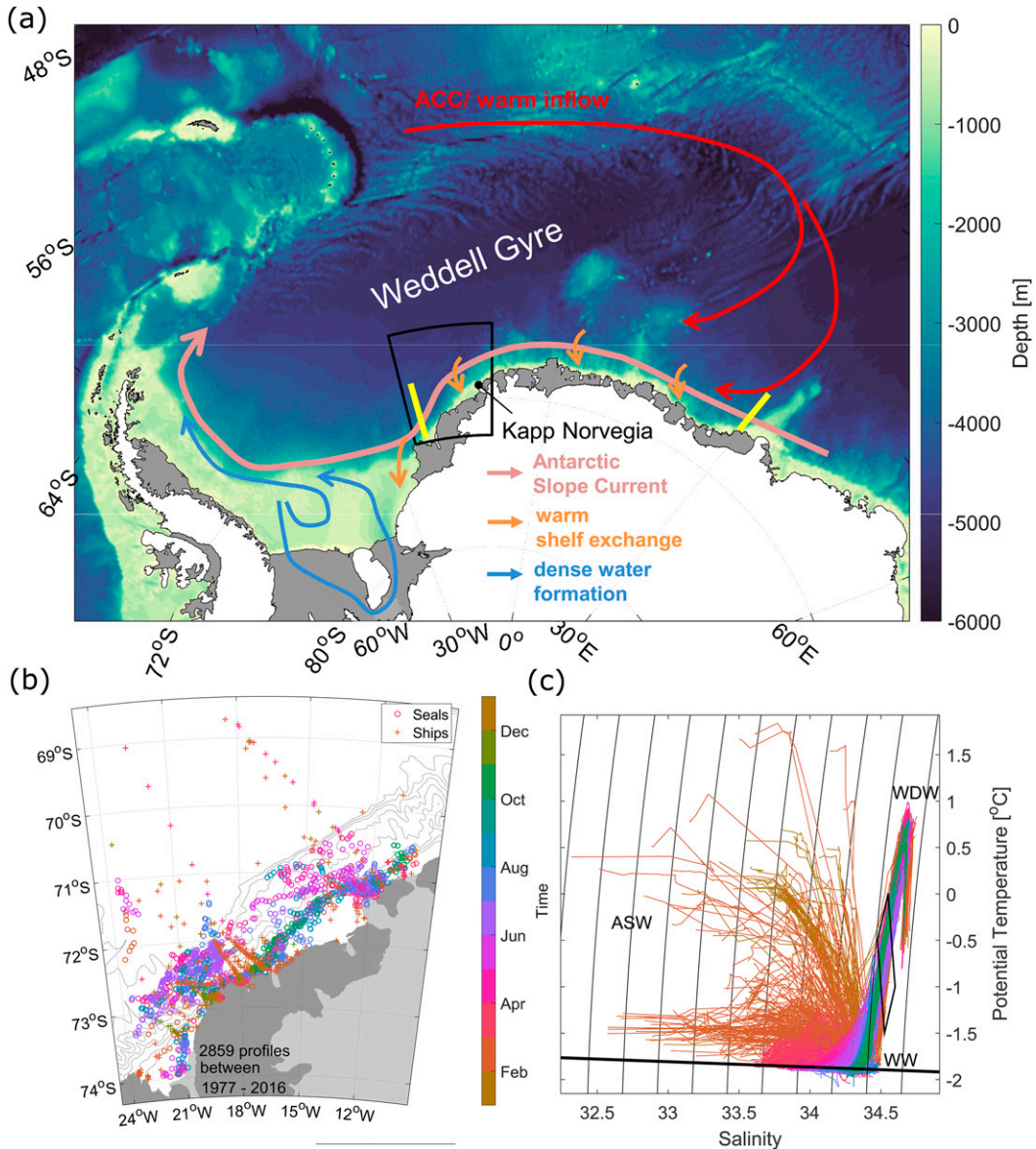
FIG. 1. (a) Map of the Weddell Gyre with arrows indicating the major circulation pathways. Yellow lines delineate the part of the boundary current that is captured by the idealized model presented in section 4. (b) Map with locations and timing (colors) of CTD profiles used for the data analysis near the continental shelf break at Kapp Norvegia. Contours show isobaths on 500-m intervals; dark gray indicates ice shelf areas and light gray indicates grounded ice and land areas in the region delineated by the black polygon in (a). (c) Potential temperature–salinity $(\theta - S)$ diagram with colors indicating the seasonal evolution of the water masses, with labels indicating the end-member properties of WDW, ASW, and WW. Contours show potential density surfaces with $0.2 \, \mathrm{kg \, m^{-3}}$ equidistance and the $27.7 \, \mathrm{kg \, m^{-3}}$ isopycnal highlighted on top of the CTD data. The sloping black line shows the surface melting point, and the polygon delineates water mass properties used to identify the thermocline depth as described in section 2b.

slope current increases (Daae et al. 2017) and the WDW thermocline becomes shallower (Hattermann et al. 2014) when being forced with summertime hydrographic conditions. To investigate whether the observed seasonal shoaling of the WDW thermocline is related to the downwelling of this ASW during summer, an idealized model of the boundary current dynamics is formulated that simulates the evolution of the thermocline depth along the shelf break as a function of wind forcing and upper ocean density changes. The model scales the thermocline depression across the ASF and predicts the seasonal shoaling and deepening of the WDW interface

TABLE 1. Overview of hydrographic datasets used to construct the climatological cross sections of the slope front.

Data source	Profiles	Start date	End date
doi:10.1594/PANGAEA.527319	8	9 Jan 1977	14 Feb 1977
doi:10.1594/PANGAEA.527410	36	6 Feb 1979	28 Feb 1979
doi:10.1594/PANGAEA.527233	2	14 Feb 1980	14 Feb 1980
doi:10.1594/PANGAEA.785904	1	20 Jan 1981	20 Jan 1981
doi:10.1594/PANGAEA.527497	1	20 Jan 1985	20 Jan 1985
doi:10.1594/PANGAEA.734977	72	23 Jan 1985	17 Feb 1985
doi:10.1594/PANGAEA.735189	63	15 Oct 1986	27 Nov 1986
doi:10.1594/PANGAEA.734988	4	26 Jan 1987	1 Feb 1987
doi:10.1594/PANGAEA.527812	7	5 Jan 1989	31 Jan 1989
doi:10.1594/PANGAEA.742579	18	11 Feb 1989	24 Feb 1989
doi:10.1594/PANGAEA.527593	7	15 Feb 1990	16 Feb 1990
doi:10.1594/PANGAEA.742577	10	15 Jan 1991	13 Feb 1991
doi:10.1594/PANGAEA.742581	2	18 Jan 1995	5 Mar 1995
doi:10.1594/PANGAEA.293960	16	30 Mar 1995	3 Apr 1995
doi:10.1594/PANGAEA.756513	13	9 Feb 1996	25 Feb 1996
doi:10.1594/PANGAEA.738489	13	25 Apr 1996	27 Apr 1996
doi:10.1594/PANGAEA.61240	1	2 Mar 1997	2 Mar 1997
doi:10.1594/PANGAEA.735530	2	24 Jan 1999	25 Feb 1999
doi:10.1594/PANGAEA.756515	25	30 Mar 2000	10 Apr 2000
doi:10.1594/PANGAEA.756517	36	5 Dec 2003	5 Jan 2004
doi:10.1594/PANGAEA.733664	13	20 Feb 2005	25 Feb 2005
doi:10.1594/PANGAEA.733414	4	15 Mar 2008	15 Mar 2008
doi:10.1594/PANGAEA.854148	11	31 Jan 2009	24 Feb 2009
doi:10.1594/PANGAEA.772244	10	24 Dec 2010	27 Dec 2010
doi:10.1594/PANGAEA.770000	17	20 Mar 2011	5 Apr 2011
doi:10.1594/PANGAEA.817255	1	28 Dec 2012	28 Dec 2012
doi:10.1594/PANGAEA.859035	22	23 Dec 2015	1 Feb 2016
nare1997	119	15 Feb 1997	15 Feb 1997
MEOP-UK/ct27-W1-07	396	19 Apr 2007	16 Aug 2007
MEOP-NO/ct34-2442-08	85	21 Feb 2008	16 Mar 2008
MEOP-NO/ct34-2453	798	22 Feb 2008	30 Oct 2008
MEOP-UK/ct43-613-09	155	2 Apr 2009	12 Jun 2009
MEOP-UK/ct70–503–11	28	26 Feb 2011	19 Sep 2011
MEOP-UK/ct70–638–11	157	29 Apr 2011	7 Aug 2011
MEOP-UK/ct70–643–11	134	4 Jun 2011	29 Jul 2011
MEOP-DE/wd06–09–13	159	14 Feb 2014	1 Sep 2014
MEOP-DE/wd06–10–13	89	14 Feb 2014	21 Sep 2014
MEOP-DE/wd07–01–15	324	23 Jan 2016	5 Apr 2016

at the shelf break as response to wind and buoyancy forcing. It also reveals a self-amplifying feedback mechanism that arises when freshwater fluxes from adjacent ice shelf basal melting is included.

2. Data analysis

a. Hydrographic profiles from ships and seals

To assess the seasonal evolution of the slope front hydrography, conductivity–temperature–depth (CTD) profiles from ships and data from Satellite Relay Data Logger–equipped seals (SRDL-CTD) were collected near the continental shelf break in the region 10°–25°W, 68°–74°S (Fig. 1a). A total of 534 ship-based CTD profiles are available between 1977 and 2016, mainly from British, Norwegian, and German research cruises. Except for 119 profiles of three synoptic sections taken in February 1997

and described by Nøst and Lothe (1997), which are hosted on https://data.npolar.no, all ship-based data are accessible through PANGAEA (https://www.pangaea.de/; see Table 1 for references) together with descriptions on calibration and data quality.

The animal-borne SRDL-CTD data are hosted under the Marine Mammals Exploring the Oceans Pole to Pole (MEOP) umbrella and consist of 2325 profiles from 10 individual animals that visited the study region between 2007 and 2016. From April to August 2007, from April to June 2009, and from May to September 2011, five Weddell seals were present that had been tagged in the southern Weddell during three British campaigns. From March to November 2008, two southern elephant seals were present that had been tagged on Bouvet Island during a Norwegian campaign. From February to September 2014 and from January 2016 to April 2017,

two Weddell seals were present that had been tagged near the Drescher inlet during two German campaigns. All data are available on http://www.meop.net with individual deployment codes being given in Table 1. Only delayed mode data from the most recent database version MEOP-CTD_2017-10-01 are employed, which were consistently processed and calibrated, including adjustment of salinity (Roquet et al. 2014), corrections for thermal cell effects (Mensah et al. 2018; Nakanowatari et al. 2017), and density inversions (Barker and McDougall 2017), yielding nominal accuracies of 0.03° and 0.02°C for salinity and temperature, respectively (Treasure et al. 2017).

All profiles were inspected to confirm that measurements spanned a reasonable range between the known end members of water mass types in the study region (Fig. 1b) and exhibited plausible vertical structure. In particular, some of the older ship-based data showed significant offsets and/or density inversions near the surface, while a smaller number of the seal data showed artifacts that suggest freezing of the sensors. These data were hence excluded from the analysis. Because of the limited amount of data that can be transferred via satellite, the vertical resolution of the SRDL-CTD profiles is somewhat reduced compared to ship-based profiles [for details, see also Boehme et al. (2009)]. Manual inspection of the data suggested that the relevant vertical structure is captured in most of the cases, while a small number of profiles that suffered from low vertical resolution of the temperature gradient at the WDW interface were excluded the from the analysis. Available Argo float data were also inspected, but only very few profiles were found in the study region, as these platforms are more suitable for greater water depths in the interior gyre.

b. Analysis along bathymetric contours and thermocline detection

Based on the assumption that the position and evolution of the slope front are strongly controlled by the shelf break topography and that other geographical differences in the study region are negligible, bathymetric coordinates are used as common reference frame for analyzing the geographically scattered data. To define a consistent bathymetric coordinate that avoids biases from small-scale topographic features, a smoothed bottom topography was obtained by binning the 1-km resolution Bedmap2 bathymetry (Fretwell et al. 2013) onto a 5 km × 5 km regular grid. The average depth of all points in a respective grid cell was then assigned as the cell's nominal bathymetric depth for the hydrographic profiles that were binned onto the same grid. Furthermore, all profiles were interpolated linearly onto a uniform vertical depth coordinate with regular spacing of 5 m to simplify further analysis.
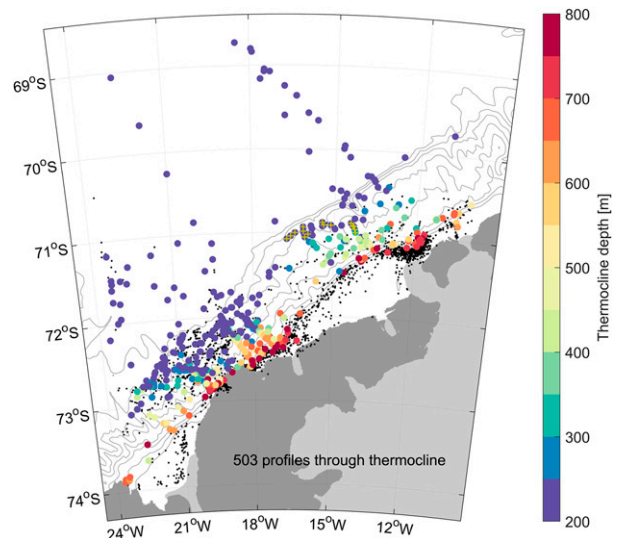

FIG. 2. Same map as in Fig. 1b with colors indicating the upper depth of the WDW layer in profiles where a thermocline was identified. Crosses indicate outliers that were excluded from the analysis as described in section 3a. Black dots indicate remaining profiles without a thermocline.

In 503 profiles a thermocline was present (Fig. 2). Its depth was determined as the depth of the modified WDW layer (the mixing product of the shelf water masses and the WDW), that is, the median depth at which water mass properties were inside a polygon defined by the θ–S pairs (34.45; −0.5°C), (34.50; 0.0°C), (34.6; −1°C), and (34.55; −1.5°C) (Fig. 1b). In about 90% of the profiles that extended into the WDW layer, the standard deviation of the vertical points that met this criterion was less than 20 m, which indicates that the modified WDW is confined to a relatively thin layer in the study region.

Most of the thermocline depth estimates are obtained from ship-based data, which are heavily summer biased. The SRDL-CTD profiles also cover the winter months, but the vast majority of the profiles were located over the continental shelf and fewer than 10% of all dives reached the thermocline. The temporal distribution of the profiles is summarized in Table 2, with about half of the thermocline depth estimates being concentrated in December through February.

c. Construction of monthly and seasonal cross sections

Combining the ship-based observations and seal data for the entire time period, at least a hundred individual profiles are available for every month of the year except November ($n = 44$) and December ($n = 34$). Based on these data, monthly mean cross sections were constructed that indicate the seasonal evolution of the slope

TABLE 2. Number of available CTD profiles in different months, with the number of ship-based profiles shown in parentheses.

Month	All profiles	Profiles through the thermocline
Jan	148 (110)	58 (58)
Feb	501 (250)	190 (160)
Mar	424 (32)	23 (16)
Apr	312 (45)	76 (21)
May	345 (0)	24 (0)
Jun	392 (0)	37 (0)
Jul	279 (0)	5 (0)
Aug	167 (0)	26 (0)
Sep	100 (0)	2 (0)
Oct	113 (19)	25 (13)
Nov	44 (44)	23 (23)
Dec	34 (34)	14 (14)

front above the WDW thermocline and are available as an individual dataset on PANGAEA (Hattermann and Rohardt 2018).

Profiles for each month were sorted along their bathymetric coordinate in 15 bins of 160-m bin size down to 2240-m water depth and 5 bins of 500-m bin size below that depth. The bin size was chosen to balance the resolution over the steeply sloping shelf break topography while maximizing the number of profiles in each bin. Profiles in each bin were averaged on their uniform vertical coordinate and combined into three-dimensional arrays for temperature and salinity as a function of bottom depth/isobath across the shelf break and time. Data gaps for months where no profiles existed in certain depth bins were filled by linear interpolation along the time dimension. A smooth and continuous surface was then fit to the cross section data in each time slice, using the MATLAB function gridfit[2] (D'Errico 2006).

Data below the thermocline are sparse during winter and the monthly cross sections mainly serve to assess the seasonal evolution of water mass properties in the upper part of the water column, where SRDL-CTD data provide good coverage year-round. To provide a more robust full-depth estimate of seasonal variations of the frontal structure, a second set of cross sections was constructed, using the same method but combining all data from July through December (winter) and all data from January through June (summer). For these sections, more than 10 profiles extending below the thermocline are available within each depth bin and time slice.

---

[2] The surface fitting is based on an algorithm that minimizes the potential energy of a system in which a thin flexible plate is connected through springs to the data points. The smoothness of the result is then determined by the relative stiffness of the plate, as compared to the strength of the springs that connect with the data, here using a smoothness parameter of 6.

For mapping the bathymetric coordinate ξ back to horizontal distance D along a cross section $\xi(D)$, a mean shelf break profile was constructed. A characteristic slope $S(\xi)$ was defined by averaging the topographic gradient associated with each CTD profile that fell in the respective bathymetric bin. A mean shelf break profile as function of distance from the coast was then obtained by integrating the characteristic slope along the bathymetric coordinate [i.e., inverting the expression $D(\xi) = \int S^{-1} d\xi$].

d. Supporting mooring time series

Time series from two moorings that were deployed along the shelf break at different times and locations provide a regional context for the seasonal variability seen in the hydrographic data. Near-bottom temperature is available from February 2007 to July 2009 at the shelf edge at 30°W in the Filchner Trough region about 500 km downstream of the study region (Årthun et al. 2012), being referred to as S4E data hereafter. A second temperature time series is available from an instrument that was deployed in the study region at 17°W from February 2009 to February 2010 close to the thermocline position at about 500-m depth over the 100-m isobath of shelf break (Graham et al. 2013), referred to as SASSI data hereafter. Both time series show a consistent seasonal cycle, with the highest temperatures appearing during a core period between January and April in the records.

The time series of the mooring temperatures are shown in Fig. 10, and will be discussed in greater detail together with the model analysis in section 4.

3. Seasonal cycle of the slope front structure

a. Variability of the thermocline depth

The map of the thermocline depth distribution shown in Fig. 2 confirms a coherent deepening of the WDW toward shallower water depth in a narrow band all along the shelf break. Condensing the along-slope dimension by projection onto the bathymetric coordinate, Fig. 3a shows the thermocline depth distribution as a function of isobaths. Colors indicate the respective month of the individual measurement. Although the data are widely scattered, a tendency of shallower thermocline depths in March/April (magenta/red) and a deeper values in November/December (green/blue) is apparent, in particular in the range of the 1500–3000-m isobaths.

An "average thermocline depth" (black curve in Fig. 3a) was constructed by sorting and averaging the individual data points into 100-m bathymetric bins and subsequent smoothing with a 15-point Hanning window running-mean filter. To estimate the deviation from the mean state, the "thermocline anomaly" was defined as
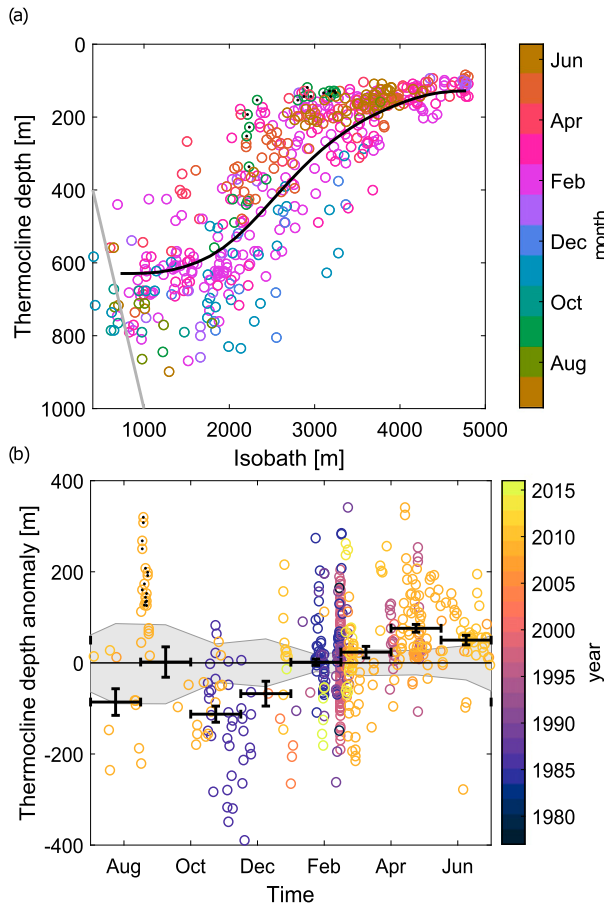
FIG. 3. (a) Thermocline depth from individual profiles shown as function of isobaths across the shelf break and for different times of the year. The black curve shows the average thermocline depth constructed as described in section 3a. The gray line shows where the thermocline depth (*y* axis) is equal to the isobath (*x* axis). (b) Seasonal evolution of thermocline depth anomaly, defined as the difference between individual profiles and the black curve in (a), with positive values indicating a shallower thermocline during April and colors indicating the year of the individual measurement. Black markers show the 60-day window with whiskers indicating the standard error $s/\sqrt{N}$, where s is the standard deviation and N is the number of measurements in the respective bin. The gray envelope indicates the $p = 0.01$ confidence interval in each bin, obtained from the Monte Carlo method explained in section 3a. Black dots in both panels indicate outliers that were excluded from the analysis as described in section 3a.

the difference between the individual measurements and the average thermocline depth at the respective isobath. Positive values in Fig. 3b show a shallower thermocline in April than in November, with the 45-day bin average indicating a rise of more than 100 m over the 6-month period. To assess the statistical significance of this seasonality, confidence intervals were estimated for each bin, based on the 99% percentile of the

thermocline anomalies in 10 000 random samples taken from the entire dataset and of equal sample size as the number of data points in the respective bin (Laken and Čalogović 2013). While the shoaling of the thermocline during summer appears to be a robust result (also for different bin sizes), for the remainder of the year where fewer data points exist the bin-averaged anomalies and their standard error estimates remain within the uncertainty range.

In particular, 15 profiles stand out that show a shallow thermocline depth during four consecutive days from September 2008 (marked with yellow crosses in Fig. 2 and black dots in Fig. 3) and located in close proximity to each other between the 200-m and 3000-m isobaths. Because of their strong influence on the overall statistics, these autocorrelated points were excluded from the analysis, since it is unclear whether they represent a true seasonal signal or rather capture a singular event during an otherwise sparsely sampled period. Since the SRDL-CTD data transmission is limited and the animals may travel a few tens of kilometers during one day, the exact positioning of individual profiles over the steeply sloping topography in ice-covered conditions is also difficult to ascertain, and in particular the data from deeper and hence longer dives may have greater positioning errors than the ship-based data. The finding of a rising thermocline between November and May, however, is robust regardless of whether or not the SRDL-CTD profiles are included.

Already Fahrbach et al. (1992) noted that temperature and salinity maxima are deeper in winter than in summer, and the thermocline depth maximum in October and November in Fig. 3b is actually derived from the same data. Evidence that this deep anomaly results from seasonal changes, rather than reflecting long-term trends or interannual variability, is provided by the February data from the same season as well as from earlier years consistently showing a shallower thermocline (color coding in Fig. 3b) than the late winter samples. Various null hypotheses were tested to scrutinize the relationships found between any parameters and the bathymetric coordinates. Neither the year of observation nor longitude or latitude shows a similar coherent pattern as can be seen for the seasonal ordinate. Moreover, the thermocline anomaly derived here is in phase with the seasonal warming seen in the SASSI data and downstream in the S4E data, indicating a coherent evolution of the slope front structure along a larger portion of the shelf break.

b. Sea ice meltwater cycle and frontal instability

During summer, prevailing onshore Ekman transport accumulates buoyant Antarctic Surface Water (ASW)
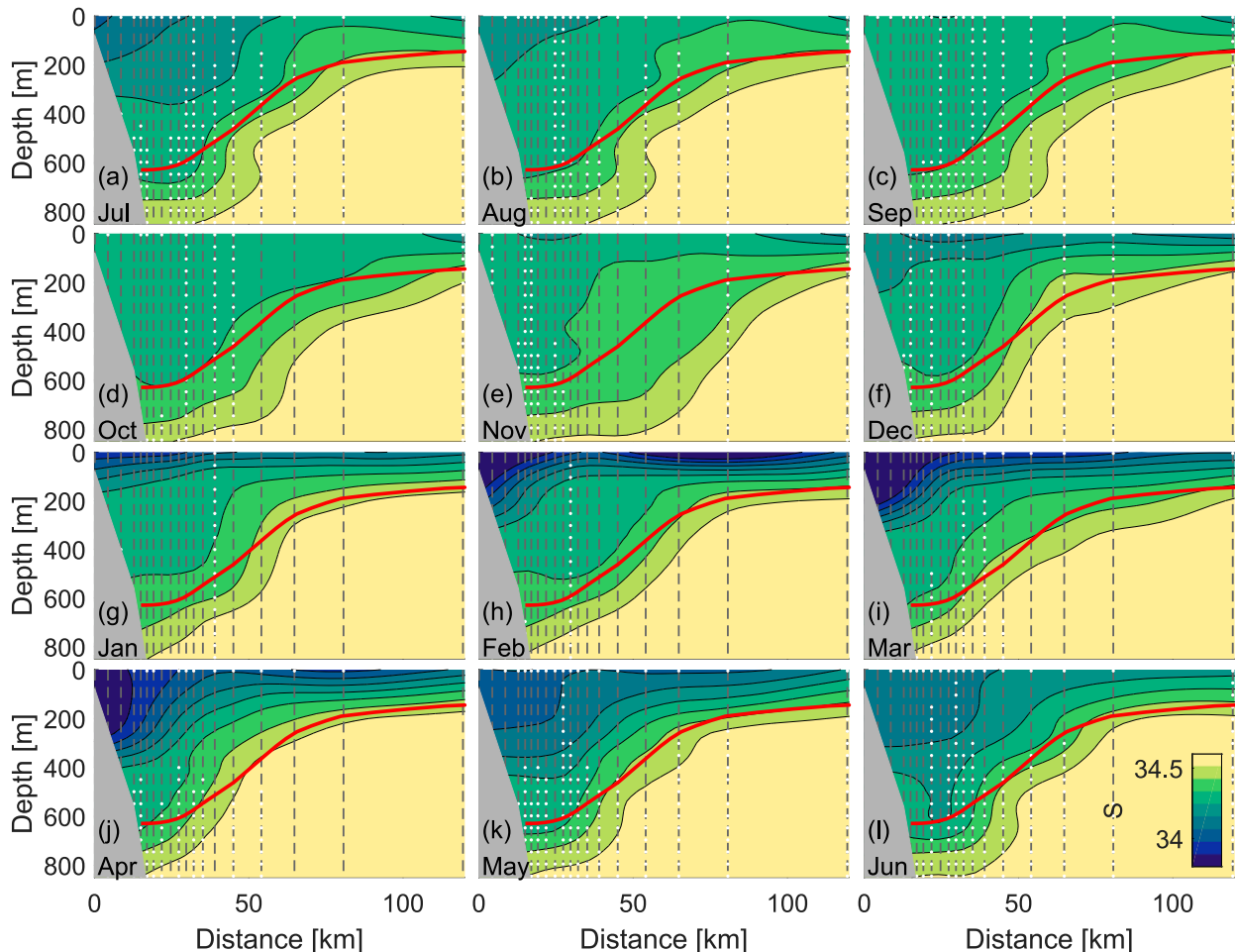
FIG. 4. (a)–(l) Monthly climatologies of salinity constructed and projected onto standard cross section as described in section 2c. Dashed vertical lines indicate the spacing of individual depth bins, white dots indicate missing data, and the red curve shows the average thermocline depth from Fig. 3a as a constant reference in each panel.

produced by sea ice melting along the eastern Weddell Sea coast. The buoyancy budget above the thermocline is to a large extent determined by downwelling of ASW into the winter water (WW) from the previous season, while freshwater input from ice shelf basal melting is limited year-round (Zhou et al. 2014; Hattermann et al. 2014). In winter, shelf water masses are convectively mixed through brine rejection during sea ice freezing (Nicholls et al. 2009), but without significant formation of dense water in this region that could penetrate below the WDW interface (Fraser et al. 2012).

The monthly climatologies of salinity and temperature in Figs. 4 and 5 show the spatial structure of the sea ice meltwater signal. From December to February, a fresh surface layer with salinities below 34.0 is formed in the upper tens of meters on top of the homogeneous WW with salinities around 34.4. While the lowest salinities in December are seen offshore (approximately over the 3000-m isobath), the freshening signal propagates onshore and successively deepens, until May, when salinities decrease to 34.2 down to 300-m depth on the continental shelf.

The temperature fields in Fig. 5 show that the upper ocean freshening is concurrent with the shoaling of the WDW. The density difference between the end members of the ASW and the WW is about 5 times larger than the density difference between the WW and the WDW (Fig. 1), and it is obvious that the seasonal evolution of the upper ocean hydrography has a strong influence on the baroclinic structure of the frontal current. To quantify this effect, the potential density fields σ_θ associated with the seasonal cross sections (Fig. 6) were used to compute the Buoyancy frequency $N^2 = -g\sigma_\theta^{-1}\partial_z\sigma_\theta$, the thermal wind vertical shear $\partial u/\partial z = g(\rho_0 f)^{-1}\partial_y\sigma_\theta$ (assuming an f plane with
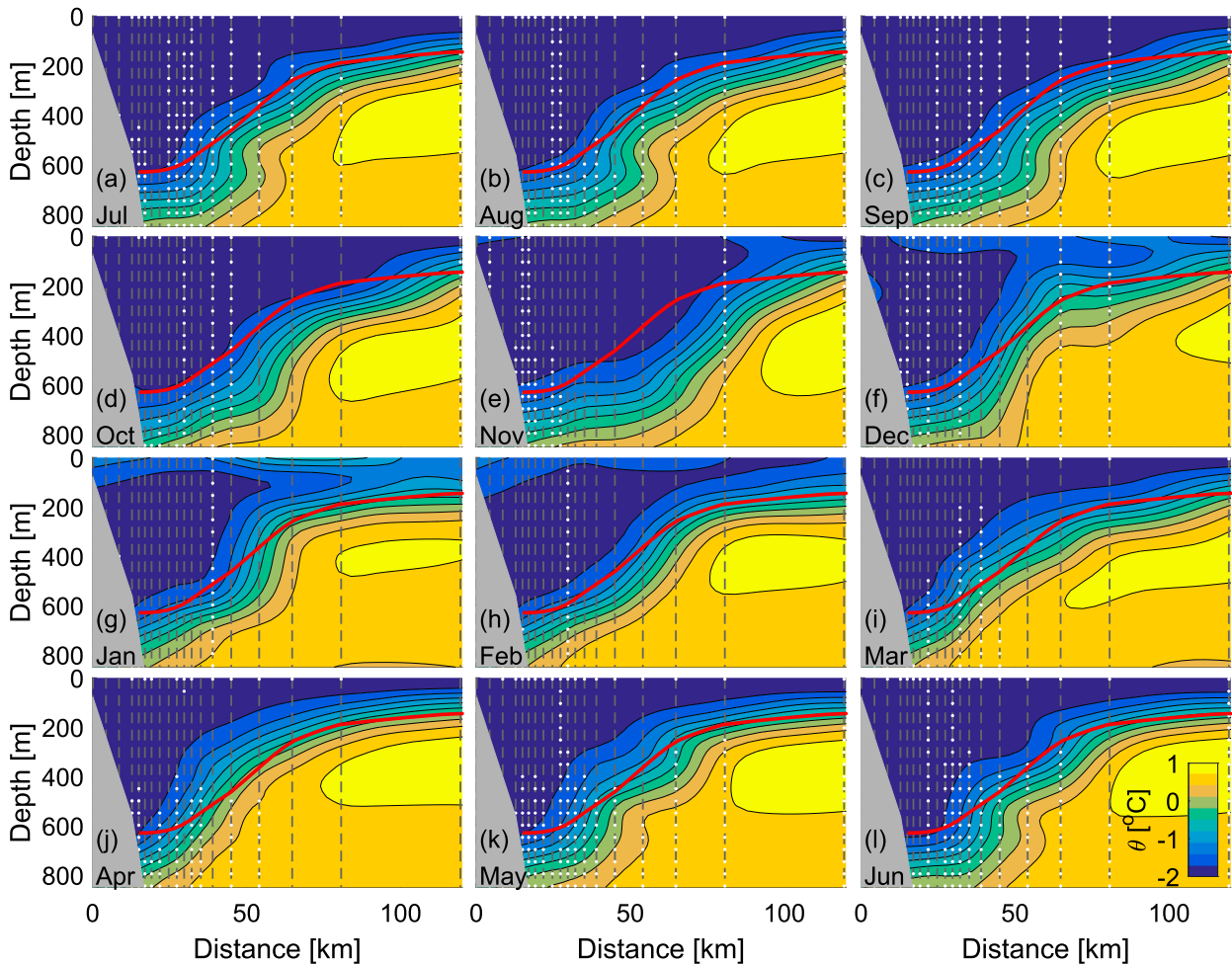
FIG. 5. As in Fig. 4, but for potential temperature.

$f = -1.38 \times 10^{-4} \, \text{s}^{-1}$), and the Richardson numbers[3] $\text{Ri} = N^2 (\partial u/\partial z)^{-2}$. The latter provides a proxy of the stability properties of the frontal current and can be used to estimate baroclinic eddy growth rates $\omega = \sqrt{0.09 f^2/\text{Ri}}$ (Eady 1949) that are shown in Fig. 7.

In winter (Fig. 7a) a wide slope current is centered over the 1500–2000-m isobath that is associated with the density gradient at the WW/WDW interface and with maximum thermal wind velocities of about 12 cm s^{-1}. This pattern is somewhat intensified in summer (Fig. 7c),

but in addition a narrow core of maximum shear velocities above 30 cm s^{-1} appears near the shelf edge, which is comparable in magnitude and structure with the summer observations of Heywood et al. (1998). While growth rates on the order of 1 day^{-1} at the WDW thermocline suggest eddy formation at the WDW interface in both seasons, the most rapid unstable growth is associated with this secondary front that develops in the upper ocean during summer. The ratios between summer and winter stratification and vertical shear (Figs. 7b,d) show that although the freshening above the thermocline stabilizes the current by strengthening the stratification, the overall effect of the downwelling of ASW is dominated by enhanced shear that enhances unstable growth at the shelf break edge. The enhanced instability suggests that the momentum input from wind that suppresses the WDW along the shelf break is partially dissipated by eddies, which are associated with the secondary front that builds up available potential energy

---

[3] The terms N^2 and $\partial u/\partial z$ were computed on a regular y–z grid with 50-m horizontal and 5-m vertical resolution and applying a simple convective adjustment algorithm to assure stability of the water column. The fields shown in Fig. 7 were smoothed by first removing all negative values and then applying a 6×6 window median filter that also fills missing values that are smaller than the window size. Also the fields for which ratios are shown in Fig. 7 were filtered using the same method.
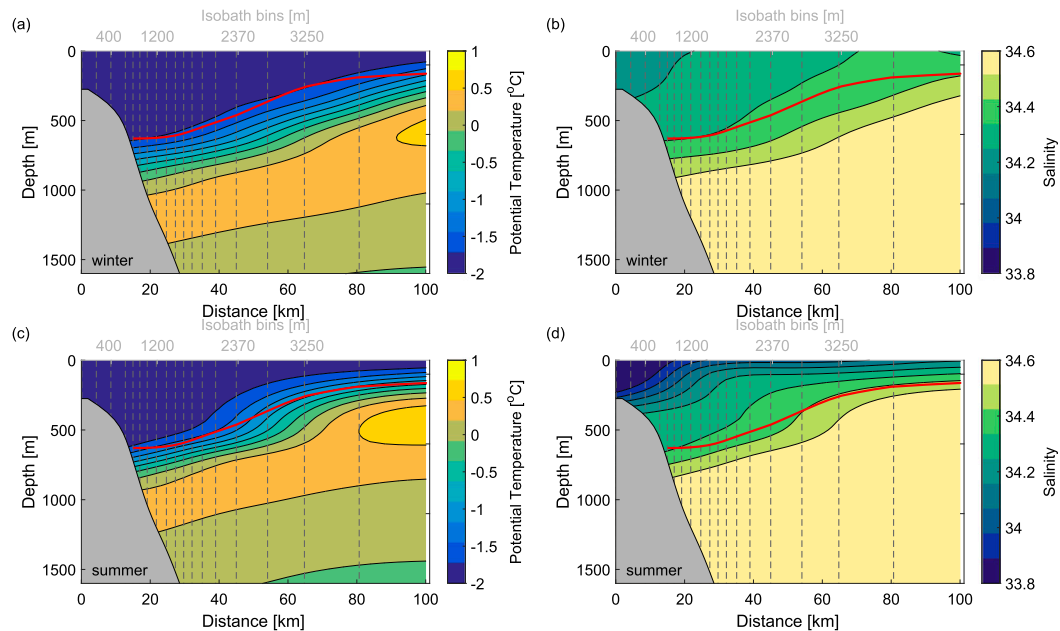
FIG. 6. Seasonal climatologies of winter (July–December) and summer (January–June) of (a),(c) potential temperature and (b),(d) salinity constructed and projected onto standard cross section as described in section 2c. Dashed vertical lines indicate the spacing of individual depth bins; the red curve shows the average thermocline depth from Fig. 3a as a constant reference in each panel.

at the ASW and WW interface. Consistently, the successive water mass transformation and associated propagation of the freshening signal to depth indicates that energy is provided for mixing between the ASW and WW on a seasonal time scale, as would be achieved by genesis of those eddies.

The simple scaling of frontal instability based on Ri does not take into account the effects of the sloping topography (Isachsen 2011) or other dynamic effects, such as barotropic instability or interactions with the bottom Ekman layer. Similar growth rates and seasonal differences were also found when applying a two-layer shallow-water model (Teigen et al. 2011) or one-dimensional stratified quasigeostrophic linear theory (Smith 2007) to the same velocity and density fields. However, because of the poor constraints on the input data, not much additional insight was gained from these more comprehensive analyses.

4. Shelf break overturning model

The analysis in section 3 suggests a relationship between the shoaling of the thermocline and the downwelling of the ASW during summer. Next, an idealized model of the slope front dynamics is constructed to assess the combined effect of wind and hydrographic forcing along the eastern Weddell Sea shelf break. The model captures the portion of the slope current that is

marked by the yellow lines in Fig. 1a, representing the southeastern limb of the Weddell Gyre. Section 4a introduces the essential elements of the frontal overturning and derives the basic model formulation. Section 4b provides an overview of the model input parameters and forcing. Section 4c investigates the sensitivity of the thermocline depth under steady-state conditions. Section 4d presents results from time-varying seasonal cycle simulations. In section 4e the effect of basal ice shelf melting is added to the model, introducing a possible tipping point behavior that is further investigated with transient upper-ocean freshening projections in section 4f.

a. Two-layer formulation of the slope front dynamics

A shelf break overturning model is derived based on the semi-enclosed, two-layer system that was used by Straneo (2006) to simulate the convective overturning in the Labrador Sea. It includes an interior region where no net mean flow occurs and a boundary current region, where properties are advected along the perimeter of the basin (Fig. 8). Both regions consist of two homogeneous layers: a light water mass with density ρ_1 that represents the WW/ASW, and a dense water mass with density ρ_2 that represents the WDW. The boundary current and interior interact at the lateral interface through eddy fluxes that are parameterized by differences in layer thickness between the two
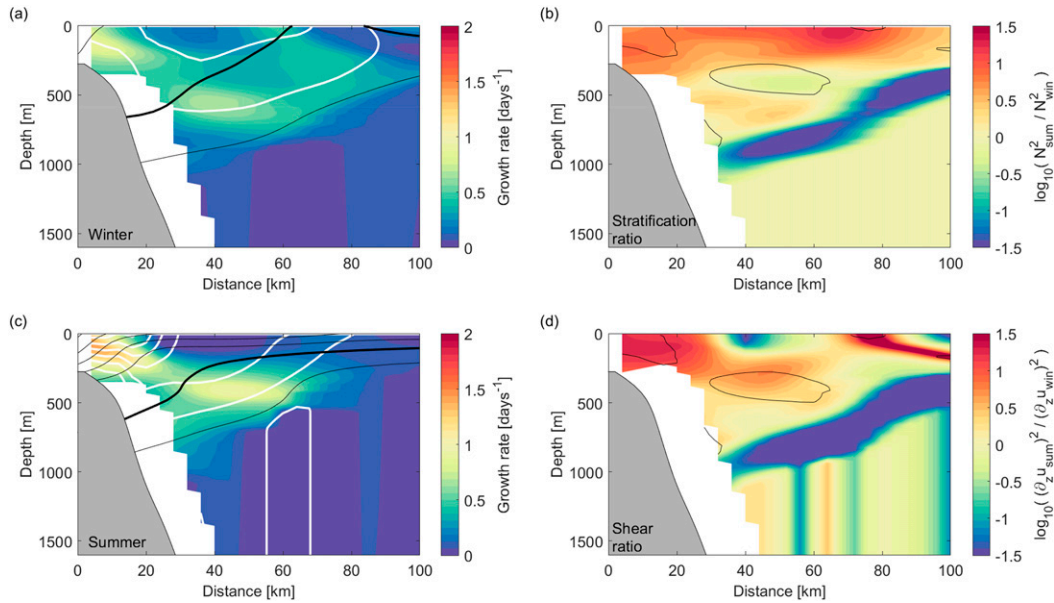
FIG. 7. Seasonal variability of slope front stability properties, showing (a) July–December and (c) January–June baroclinic growth rates (color), thermal wind shear velocity (white contours; $5\,\mathrm{cm\,s^{-1}}$ interval), and potential density contours (black; $0.1\,\mathrm{kg\,m^{-3}}$ interval; and $27.7\,\mathrm{kg\,m^{-3}}$ isopycnal highlighted in bold), constructed and projected onto standard cross section as described in section 2c. Also shown are the summer to winter ratio of the Richardson number (b) numerator and (d) denominator on a logarithmic scale. Black contours delineate areas where growth rates increase by a factor of 1.5 and more during summer, showing the respective stabilizing (destabilizing) effect of increased stratification (vertical shear) over the shelf break.

regions. The main forcing in the Labrador Sea case was set by dense water formation through surface heat loss in the interior, which was compensated by an eddy heat transport from the boundary current. For the Weddell Sea case instead, a wind-driven Ekman overturning circulation is imposed that advects lighter water at the surface from the interior into the boundary current, with a net volume flux that is balanced by a return flow at depth. This Ekman overturning continuously deepens the layer interface in the boundary current, which is balanced by an opposed eddy overturning that compensates the buoyancy loss from the interior and transports dense water into the boundary current. Herein, it is assumed that the bottom Ekman flow is a result of the barotropic current that is associated with the sea surface elevation gradient caused by the convergence of the surface Ekman transport along the coast (Sverdrup 1953) and that there is no net volume flux associated with the Ekman overturning and the eddy overturning, respectively. Additional surface buoyancy fluxes (i.e., due to gradients in precipitation) are neglected and assumed to linearly superimpose onto this balance.

Following the notation and geometrical considerations of Straneo (2006) (an overview of model parameters and constants is given in Table 3), a cylindrical basin is assumed with radius R, total depth H, interior area $A = \pi R^2$, and a boundary current of thickness L and total perimeter P. The variables of the system are the interior's dense water thickness $D(t)$ and the boundary layer thicknesses $h_1(l, t)$ and $h_2(l, t)$ and velocities $V_1(l, t)$ and $V_2(l, t)$, where t denotes the time dependency of the variables and l is the along-boundary coordinate ranging from 0 to P (Fig. 8). Based on this, a conservation equation for buoyancy in the interior region is obtained, here written in terms of density for simplicity:

$$\frac{\partial}{\partial t}\int_V \overline{\rho}\,dV + \int_P\int_H \overline{u'\rho'}\,dl\,dz = \Delta\rho\int_P\int_0^{z_e} v_e\,dz\,dl. \quad (1)$$

The first term in (1) describes the total change of buoyancy integrated over the interior volume V, and the second term represents the eddy fluxes integrated along the lateral interface with the boundary current along the perimeter. The third term represents the Ekman overturning given as the integral of the wind-driven flow from the interior into the boundary current v_e over the depth of the Ekman layer z_e and the density difference between the two model layers $\Delta\rho = \rho_2 - \rho_1$.

To approximate the easterly winds that are fringing the coast in the study region, an angular wind stress with constant magnitude τ_s is assumed to be aligned with the boundary current perimeter, such that the Ekman overturning can be expressed as
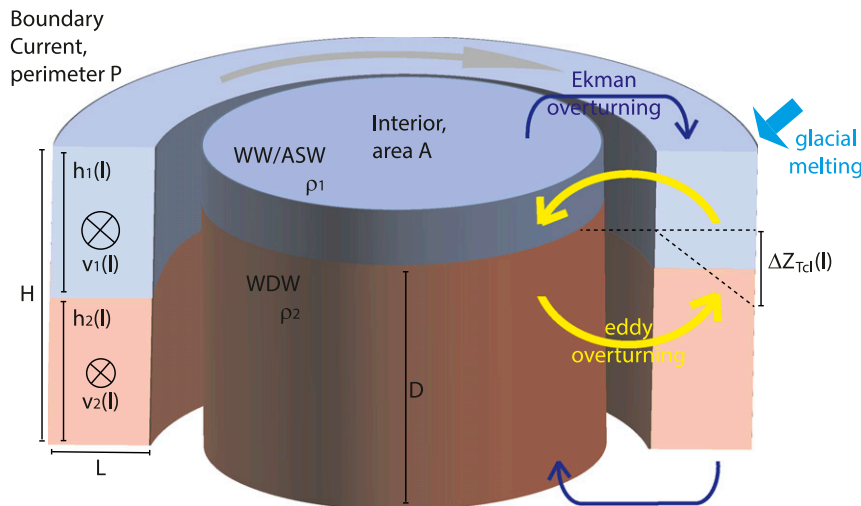
FIG. 8. Schematic of the two-layer, semi-enclosed boundary current overturning model that is used to simulate the thermocline evolution along the shelf break as a function of coastal buoyancy fluxes. The corresponding extent of the model boundary current is marked by the yellow lines in Fig. 1.

$$\int_P \int_0^{z_e} v_e \, dz \, dl = -\frac{\tau_s}{\rho_0 f} P = V_e. \tag{2}$$

Eddy fluxes are assumed to be proportional to the isopycnal slope (Spall 2004) and are parameterized as a function of the baroclinic flow magnitude $v^* = 2g'H/(fL)$ to act over the step joint where the dense water in the interior is in lateral contact with the light water in the boundary current:

$$\int_H \overline{u'\rho'} \, dz = c\Delta\rho v^* \frac{(D-h_2)^2}{H}, \tag{3}$$

where c is an efficiency constant (Spall and Chapman 1998) and $g' = g\Delta\rho/\rho_0$ is the reduced gravity of the two-layer system.

Formulating the first term in (1) for a two-layer system and substituting the expressions (2) and (3), a prognostic equation for the interior dense water layer thickness is obtained:

$$\frac{dD}{dt} + \frac{v^*c}{AH}\int_P (D-h_2)^2 \, dl = \frac{V_e}{A}. \tag{4}$$

Based on the derivations outlined in section 3c of Straneo (2006), a similar expression for buoyancy conservation in the boundary layer is formulated,

$$L\Delta\rho \frac{\partial h_2}{\partial t} + L\Delta\rho \frac{\partial}{\partial l}(V_2 h_2) = -\int_H \overline{u'\rho'} \, dz - \Delta\rho \frac{V_e}{P}, \tag{5}$$

stating that the total change in buoyancy on the LHS is given by the eddy fluxes and the Ekman overturning as

derived in appendix A. Separating the divergence term and substituting for the eddy fluxes, the prognostic equation for the evolution of the dense water layer thickness in the boundary current becomes

$$\frac{\partial h_2}{\partial t} + V_2 \frac{\partial h_2}{\partial l} + h_2 \frac{\partial V_2}{\partial l} = \frac{v^*c}{HL}(D-h_2)^2 - \frac{V_e}{LP}. \tag{6}$$

Assuming that the flow is always geostrophically adjusted, expressions for the upper- and lower-layer velocities are

$$V_1 = V_{btp} + \frac{h_2}{H}V_{bcl} \quad \text{and} \quad V_2 = V_{btp} - \frac{h_1}{H}V_{bcl}, \tag{7}$$

with the baroclinic velocity $V_{bcl} = v^*(D-h_2)/H$, where $v^* = 2g'H/(fL)$ characterizes the magnitude of the baroclinic flow, and a depth-averaged barotropic component $V_{btp} = (V_1 h_1 + V_2 h_2)/H$.

Analogous to the isopycnal slope used in (3), the shoreward depression of the thermocline $\Delta z_{tcl} = 2(D-h_2)$ is diagnosed from the difference in mean layer depth taken to represent a linearly sloping interface across the boundary current that is continuous at the interface with the interior basin (Fig. 8). Note that Δz_{tcl} describes the relative difference between the depth of the dense water layers in the interior and in the boundary current, which appears to be more useful for the sensitivity studies shown here than the absolute thermocline depth, which also depends on the layer depth in the interior.

In reality, heat and freshwater fluxes will affect the density of the surface layer together with diapycnal

TABLE 3. Model parameters and constants.

Parameter	Symbol	Units	Value
Reference density	ρ_0	kg m^{-1}	1027
Upper-layer density, WW/ASW	ρ_1	kg m^{-1}	
Lower-layer density, WDW	ρ_2	kg m^{-1}	
Layer density difference	$\Delta\rho = \rho_2 - \rho_1$,	kg m^{-1}	
Reduced gravity	$g' = \dfrac{g\Delta\rho}{\rho_0}$	m s^{-2}	
Topographic efficiency coefficient (Spall and Chapman 1998)	c		0.03
Total basin depth	H	m	2500
Basin radius	R	m	800×10^3
Boundary current width	L	m	75×10^3
Boundary current perimeter length	P	m	2000×10^3
Basin area, assuming cylindrical geometry	$A = \pi R^2$	m^2	
Coordinate along the boundary current	l	m	$[0, P]$
Interior dense water thickness	$D(t)$	m	
Boundary current upper-layer thickness	$h_1(l, t)$	m	
Boundary current lower- layer thickness	$h_2(l, t)$	m	
Boundary current upper-layer velocity	$V_1(l, t)$	m s^{-1}	
Boundary current lower-layer velocity	$V_2(l, t)$	m s^{-1}	
Magnitude of the baroclinic flow	$v^* = \dfrac{2g'H}{fL}$	m s^{-1}	
Thermocline depression across the front	$\Delta z_{\text{tcl}} = 2(D - h_2)$	m	
Surface momentum stress	τ_s	N m^{-2}	
Climatological mean surface stress	τ_0	N m^{-2}	0.072
First annual mode surface stress	τ_{12}	N m^{-2}	0.026
Ekman overturning volume transport	$V_e = -\dfrac{P}{\rho_0 f}\tau_s$	m^3 s^{-1}	
Boundary current volume transport	$T = L(V_1 h_1 + V_2 h_2) = T_{\max}\dfrac{\tau_s}{\tau_{\max}}$	m^3 s^{-1}	
Seasonal maximum boundary current transport	$T_{\max}$	m^3 s^{-1}	14×10^6
Total present-day glacial meltwater input along the coast	$F = P\dot{m}_0$	m^3 s^{-1}	15×10^3
Mean melting point temperature at 300-m depth	Φ_{300m}	°C	−2.11
Ice shelf melting efficiency coefficient (Nøst et al. 2011)	γ		0.3

fluxes at the layer interface. Simulating these effects would require additional prognostic equations for the layer density that are not included in the model. Instead, the density difference between the layers is prescribed by an external parameter. This separation is justified by the assumption that the eddy fluxes between the layers are mainly adiabatic (i.e., only affecting the layer thickness but not their water mass properties), which is a reasonable assumption for the ocean interior as, for example, argued by Marshall and Radko (2003). Furthermore, for the time-varying case, it is assumed that the externally imposed changes of the upper layer density are uniform in space and much larger than the diapycnal fluxes between the layers on seasonal time scales. This is justified because the summer freshening, which has the main effect on the upper layer density, relates to the accumulation of sea ice meltwater from a greater area and cannot be explained by local surface fluxes or ice shelf melting along the

coast (Zhou et al. 2014). Although advection of salinity anomalies along the boundary current has been observed (Graham et al. 2013), changes of the seasonal background field will occur uniformly along the perimeter of the model because of the synchronous annual cycle of sea ice formation and melt and coastal downwelling. Diapycnal mixing and adiabatic (submesoscale) eddy fluxes are likely to be important for the redistribution of the meltwater near the surface and in the upper water column, but the details of these processes cannot be resolved in the two-layer model and are imposed with the density evolution in the upper layer that is inferred from the observations as an external forcing.

Furthermore, the assumption of no net mean flow for the interior region may not be as valid as for the semi-enclosed Labrador Sea that the model was originally developed for. While Straneo (2006) focused on studying relationships between polar heat flux and basin wide

convection, in the Weddell Sea case changes in the interior region are considered to be less important and the model is mainly used to investigate the effect of the external forcing on the structure of the boundary current. As a consequence, the interior region primarily acts as a reservoir with a prescribed layer thickness that is assumed to be controlled by other processes that are not included in the model.

b. Input parameters and constants

The model predicts the layer interface evolution in each region and the baroclinic velocities along the boundary current as function of surface wind stress τ_s and density difference $\Delta\rho$ between the two layers. To specify the model forcing, the range of the density difference between the two layers was obtained by comparing potential density of the WDW with $\theta = 0.5°C$ and $S = 34.65$ in the lower layer with the upper ocean densities obtained from averaging potential density above the thermocline in the monthly climatologies presented in section 3b (Figs. 4 and 5).

The role of seasonal varying easterly winds is addressed by adapting the analytical expression for the first annual mode climatological wind stress along the shelf break that was derived from reanalysis data by Su et al. (2014):

$$\tau(t) = \tau_0 + \tau_{12} \sin(\omega t + 5\pi/3). \qquad (8)$$

Here, the mean stress $\tau_0 = -0.072\,\mathrm{N\,m^{-2}}$, the amplitude of the annular mode $\tau_{12} = -0.026\,\mathrm{N\,m^{-2}}$, and the frequency $\omega = 2\pi\,\mathrm{yr^{-1}}$, yielding a wind stress maximum in June and minimum in December. This estimate does not account for the effect of sea ice, which may either strengthen or weaken the momentum transfer into the ocean (Lüpkes and Birnbaum 2005) depending on the ice conditions. Su et al. (2014) also identified a secondary semiannual mode at about half of the amplitude of the annual mode and (8) should hence be regarded as first-order description of the wind-induced seasonality that is available from the literature, rather than a detailed assessment of the climatological wind field.

In addition, the geometric parameters L, H, P, and R need to be specified, as well as the prescribed depth averaged boundary current velocity V_{btp}. Dynamical length scales of $L = 75\,\mathrm{km}$ and $H = 2500\,\mathrm{m}$ of the boundary current are chosen to be representative for the cross sections seen in Fig. 6. They have no notable effect in the interior, but reducing those values increases the magnitude of the layer interface changes in the boundary current for runs with time-varying forcing. The changes equally affect the response to wind stress and density

difference, hence not altering the findings presented below. A perimeter of $P = 2000\,\mathrm{km}$ is used, which corresponds approximately to the distance between Gunnerus Ridge at 30°E and Kapp Norvegia at 17°W. Along this stretch of coast, the ASF and coastal current merge with the southern limb of the Weddell Gyre (Ryan et al. 2016) to form the coherent boundary current along the narrow continental shelf break that is represented by the model. A radius of $R = 800\,\mathrm{km}$ of the interior region is chosen and determines the inertia of the interior dense water layer thickness, but with little effect on the evolution of the boundary current layer interface.

The barotropic velocity is scaled based on the total transport $T = HLV_{\mathrm{btp}}$ of the boundary current. Heywood et al. (1998) report a summer/autumn upper bound of $T_{\max} = 14\,\mathrm{Sv}\,(1\,\mathrm{Sv} \equiv 10^6\,\mathrm{m^3\,s^{-1}})$ to be associated with the ASF. This transport is directly related to the wind forcing (Fahrbach et al. 1994; Nuñez-Riboni and Fahrbach 2009), and for consistency the transport applied in the model will be scaled with respect to the summer/autumn wind stress maximum $\tau_{\max} = \tau_0 + \tau_{12}$ from (8) for a given model forcing $T(\tau_s) = T_{\max}\tau_s/\tau_{\max}$, yielding typical depth averaged velocities on the order of 5–$10\,\mathrm{cm\,s^{-1}}$. Similar to the effect of L and H, smaller values of V_{btp} increase the sensitivity of thermocline depth in the transient simulations. But since depth-averaged currents are related to the geometry as discussed above, the model results are practically insensitive to changes of individual parameters as long as the total transport is kept constant.

The efficiency coefficient in the eddy parameterization $c = 0.03$ was adopted from Straneo (2006) and represents a midrange choice of the values that were originally proposed by Spall and Chapman (1998). A summary of all model parameters is shown in Table 3.

c. Steady-state solutions

As opposed to the Labrador Sea case, where a net buoyancy loss in the interior causes a transformation of the boundary current, the steady-state solutions for the Weddell Sea model converge toward a constant layer interface depth in the along-current direction $\partial h_2/\partial l \to 0$, at which the counteracting Ekman and eddy overturning are locally in balance. The obtained difference in interface depth Δz_{tcl} is independent of most model parameters.

Omitting the time derivatives in (4) and (6), an analytical expression for the thermocline depression is obtained:

$$\Delta z_{\mathrm{tcl}} = \sqrt{\frac{2\tau L}{cg\Delta\rho}}. \qquad (9)$$

(a)

Δz_{tcl} [m]

(b)

$(\partial_{tau}\Delta z)/(\partial_{rho}\Delta z)$

(c)

V_{bcl} [cm s^{-1}]
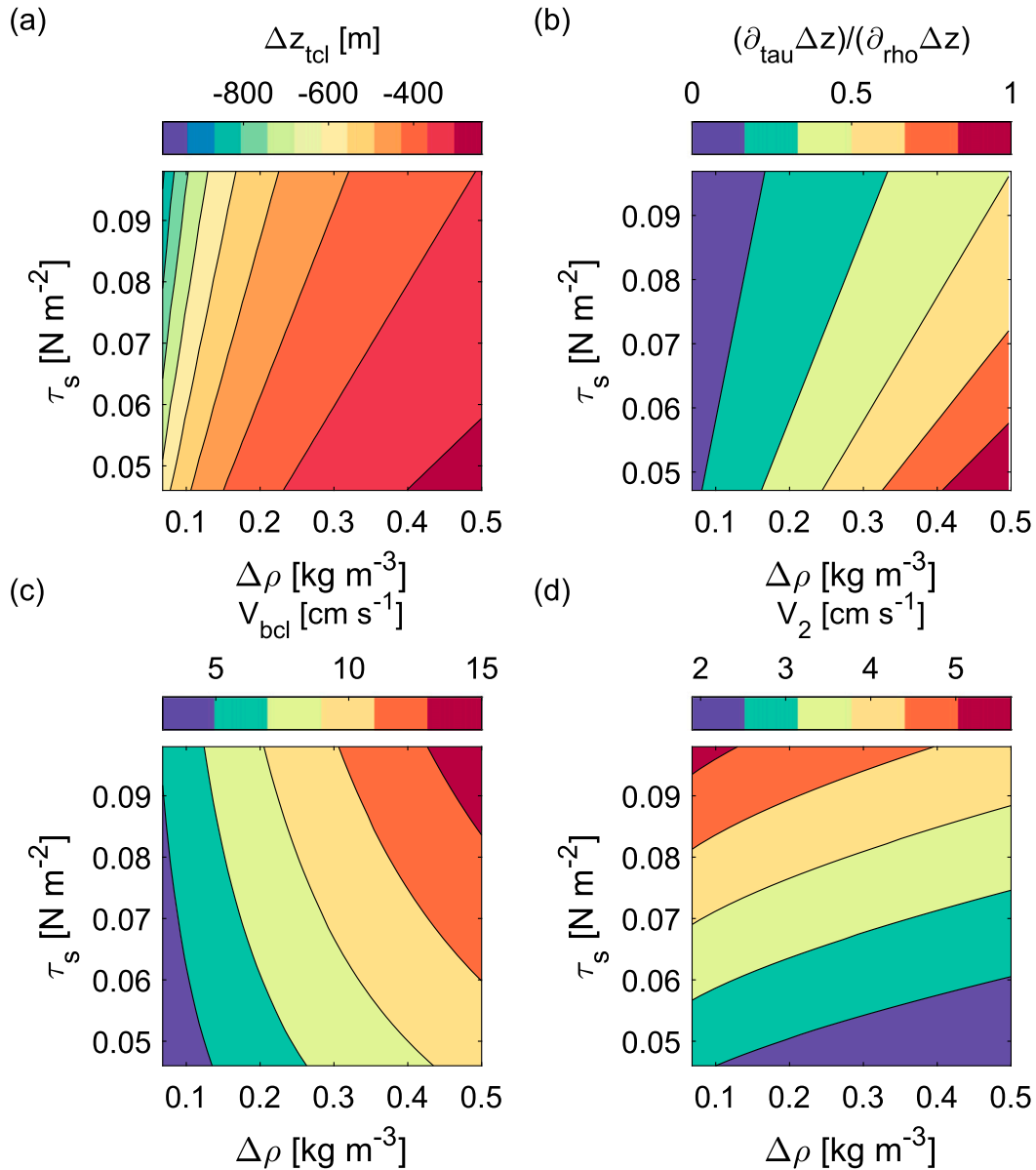

(d)

V_2 [cm s^{-1}]

FIG. 9. Steady-state solutions of (a) thermocline depression depth and (b) its relative sensitivity to wind and density forcing, as well as (c) associated baroclinic and (d) bottom layer current velocities of the two-layer system. A value of 1 in (b) means that the thermocline depth responds equally to relative changes in density and wind forcing, normalized for the parameter range shown in the figure, whereas for smaller values the sensitivity to changes in density forcing is larger.

Figure 9a shows the equilibrium thermocline depression as function of wind stress and density difference for a parameter range that is representative of the seasonal variability outlined in section 4b. Over most of the parameter range, the thermocline depression varies between 350 and 550 m (Fig. 9a). Using an annual average density difference of about $\Delta\rho = 0.25$ kg m^{-3} together with the climatological mean wind stress of $\tau_0 = 0.072$ N m^{-2} (Su et al. 2014) yields an equilibrium thermocline depression of about 380 m, which is comparable with the observed deepening of the thermocline at the shelf break of about 450 m (Fig. 3).

Equation (9) also reveals a qualitatively different response to winds and hydrographic forcing. While the thermocline deepens nearly linearly with increasing winds for the given parameter range, the deepening increases asymptotically for small density differences (Fig. 9a). The ratio of the relative importance of wind
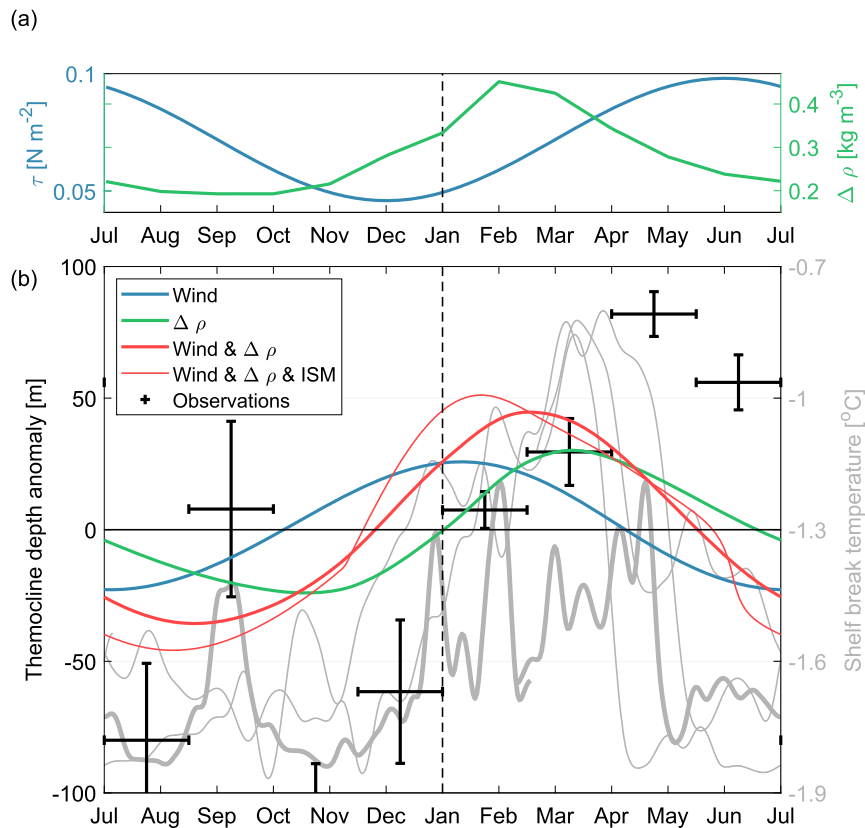
FIG. 10. (a) Annual cycle of climatological wind stress (left axis) from (8) and layer density difference (right axis) derived in section 4d used for the transient model forcing. (b) Annual cycle of thermocline depth anomaly (left axis) at the model outflow boundary from different experiments (colored curves) together with 45-day bin-averaged thermocline depth anomalies (black markers) derived from the CTD data as shown in Fig. 3b, as well as time series of shelf break temperatures (right axis) from different years of the S4E (thin gray curves) and SASSI (thick gray curve) data described in section 2d.

and hydrographic forcing[4] (Fig. 9b) shows that the sensitivity to density changes is twice as large as the response to winds for midrange values of the forcing. Only for the weakest winds and large density differences does the wind forcing become equally important (i.e., showing a wind/density sensitivity ratio close to unity).

The steady-state solutions also provide insight into the vertical structure of the boundary current (Figs. 9c,d). Considering that velocities represent layer averages, the magnitude of baroclinic currents of 10–15 cm s^{-1} for larger density differences is comparable to the thermal wind shear seen in summer (Fig. 7c). Consistently, bottom layer velocities (Fig. 9d) become minimal when

wind forcing is weak (which by construction of the input parameters also projects on the depth averaged transport) and baroclinic currents are strong.

d. Time-varying seasonal cycle

Equations (4) and (6) form two nonlinear coupled equations with two unknowns, $D(t)$ and $h_2(t, l)$. They can be solved numerically to predict the layer interface evolution in each region and the baroclinic velocities along the boundary current as function of surface wind stress τ_s and density difference $\Delta\rho$ between the two layers. Numerical methods were adopted as described in Straneo (2006), but here finding that no Laplacian diffusion was needed for stability for sufficiently small time steps in the forward difference time-stepping scheme. The spatial and temporal step size of the discretization are $\Delta x = 50$ km and $\Delta t = 10$ days respectively.

A seasonally varying but spatially homogeneous forcing is introduced (Fig. 10a), using (8) for wind stress

---

[4] Using the normalization $\partial_{tau}\Delta z = (\partial\Delta z/\partial\tau)/(\tau_{max} - \tau_{min})$ and $\partial_{rho}\Delta z = (\partial\Delta z/\partial\rho)/(\Delta\rho_{max} - \Delta\rho_{min})$, where $\tau_{max/min}$ and $\Delta\rho_{max/min}$ are the respective minimum and maximum values of the wind stress and density difference shown in Fig. 9a.

and linearly interpolating monthly mean values of the upper-layer density for the respective model time step. Furthermore, initial conditions for D and h_2, as well as boundary conditions for the eastern inflow $h_2(t, l = 0)$, must be specified. These are given by the steady-state solution obtained when time averaging the seasonal forcing. The boundary conditions are kept constant in time, such that variations in thermocline depth along the perimeter are entirely determined by internal model dynamics. From (9), it follows that the steady-state solution is independent of the interior dense water layer thickness, and in practice the time-varying runs were tuned to converge at a mean value of $D = 150$ m, which roughly corresponds to the depth of the thermocline away from the coast in Fig. 3. Seasonal changes of D in the transient runs are negligible.

To investigate the respective effect of the wind and hydrographic forcing on the seasonal evolution of the thermocline depth, three different runs were performed, where constant annual mean values are applied either for the wind stress (the $\Delta\rho$ run) or the density difference (the wind run) or both vary with time (the wind and $\Delta\rho$ run). The solutions quickly converge toward quasi-steady oscillations around the annual mean state, and Fig. 10b shows an annual composite of the simulated thermocline depth evolution at the model outflow boundary, together with the temperature series from the S4E and SASSI data and the seasonal thermocline evolution derived in section 3. All three simulations show a deepening of the thermocline in winter and a rise of the WDW in summer. However, the timing shifts in the different runs and, in particular in the wind run, the shallowest thermocline position in January appears to be too early compared to the temperature time series. Although the temperature maximum in March corresponds well with the timing of shallowest thermocline position in the $\Delta\rho$ run, the elevated thermocline position after that late peak does not match with the drop in temperatures in June. The best resemblance of the temperature signal is found when both wind and density vary, with correlation coefficients between the different model scenarios and the observations being summarized in Table 4.

The phasing of the thermocline extrema in the solely wind- or density-forced runs lags behind their respective forcings by approximately 1 to 2 months. This reflects the balance between the local forcing and the advective propagation of the seasonal signal in the model. The delay and the magnitude of the seasonal anomaly increase along the perimeter, but the effect saturates (the total advection time along the 2000-km-long boundary current is about 300 days for the given barotropic velocity) and sensitivity tests for a range of P between 1000

TABLE 4. Correlation between simulated seasonal thermocline depth evolution and observed shelf break temperature r_{Temp} and observed thermocline depth anomaly r_{Tcl}.

Forcing	r_{Temp}	r_{Tcl}
Wind only	0.54	−0.40
$\Delta\rho$ only	0.69	0.64
Wind and $\Delta\rho$	0.79	0.21
Wind and $\Delta\rho$ and ISM	0.72	0.09

and 3000 km yield a similar picture as shown in Fig. 10. In the wind and $\Delta\rho$ run, the effects of the two different forcings appear to combine additively such that the resulting thermocline evolution is in phase with the density evolution ($r = 0.98$), whereas correlations with the wind stress are weak ($r = -0.20$). Also the magnitude of the thermocline displacement increases to about 80 m when both forcings act together, which is less than but comparable to the shoaling of the WDW between December and May that is inferred from the hydrographic data.

The baroclinic current (not shown) is dominated by changes in density forcing and varies in the wind and $\Delta\rho$ run between 7 cm s^{-1} in October and 13 cm s^{-1} in February, which is consistent with the thermal wind fields inferred in section 3 for average layer velocities. The bottom layer velocity varies between 2 cm s^{-1} in February and 6 cm s^{-1} in August, being lowest in summer, mainly due to the reduced barotropic transport under the weak wind forcing, but somewhat amplified by the enhanced baroclinicity for large density gradients. This trend is in agreement with the development of a countercurrent above the seabed of the shelf break that was inferred from CTD data in summer (Heywood et al. 1998; Chavanne et al. 2010). In fact, the bottom layer current also temporarily reverses in the model when the total transport of the boundary current is reduced in the setup.

Eventually, none of the model runs fully captures the seasonality suggested by the observations. In particular the scattered CTD-based thermocline depth estimates are only weakly correlated with the model, which seems to underestimate the overall magnitude and lead the phase of the thermocline anomaly in the wind and $\Delta\rho$ run. The overall correspondence of the CTD-based seasonality with the temperature time series from three years at the Filchner Trough and from one year at Kapp Norvegia provides some evidence of a coherent pattern along the slope. Thus, the mismatch may be explained by the idealized forcing and other model simplifications (e.g., condensing the upper ocean density evolution into a single layer). However, the observational estimates remain too uncertain to assess the differences in detail (e.g., showing substantial interannual variability in the mooring time series), highlighting the

need for better observations of the thermocline depth variability, in particular during the winter.

e. Ice shelf melting feedback and multiple steady states

The sensitivity of the thermocline depth to changes in cross-frontal density difference implies a positive feedback, where freshening along the coast due to increased basal melting of ice shelves may lead to shoaling of the WDW. This allows warm water to access the shelf, which in turn further amplifies basal melting. Observations and models suggest that Antarctic surface waters will continue freshening in the future because of increased precipitation and less sea ice formation (de Lavergne et al. 2014), and the warming scenario of Hellmer et al. (2017) suggests that a sudden rise of the WDW in the Southern Weddell Sea could trigger a shift toward a warm state and significantly increased ice mass loss.

To assess whether such a regime shift may be affected by a melting feedback upstream, the effect of ice shelf basal melting along the eastern Weddell Sea coast is added to the slope front overturning model. The model formulation in (6) assumes that the Ekman and eddy transports are perfectly balanced. Meanwhile eddies may induce a residual overturning and associated cross-front transport when a net buoyancy forcing is imposed to the system (Marshall and Radko 2003; Stewart and Thompson 2016). Observations and models suggest that eddies cause an up-slope transport at the eastern Weddell Sea shelf break that provides heat for melting into the ice shelf cavities (Nøst et al. 2011). Numerical models show that the efficiency of this mechanism directly relates to the buoyancy input from ice shelf melting (see appendix B; see also, e.g., Zhou et al. 2014).

To represent this effect in the model formulation, (3) is augmented to

$$\int_H \overline{u'\rho'}\, dz = c\Delta\rho v* \frac{(D - h_2)^2}{H} + B_{\dot{m}}(h_2). \qquad (10)$$

The second term on the right-hand side in (10) represents a residual eddy transport, which compensates the buoyancy flux that is imposed by the freshwater input $\dot{m}$ from ice shelf melting:

$$B_{\dot{m}}(h_2) = -\dot{m}(\rho_0 - 1000). \qquad (11)$$

Remote sensing estimates (Rignot et al. 2013) suggest that basal melting at the ice shelves between 30°E and 20°W (i.e., from Roi Bauduoin Ice Shelf to Brunt Ice Shelf) accounts for a total mass loss of 70 Gt per year. This corresponds to a freshwater input of about $F = 2.2$ mSv, which is translated into a local flux $\dot{m}_0 = F/P$ that is taken

to be uniformly distributed along the model perimeter. It is assumed that a transition takes place where the thermocline rises above the shelf break, causing direct access of WDW to ice shelf cavities. A zero-order estimate of the melting increase by the WDW inflow is obtained by scaling melt rates with the change in thermal driving (Beckmann and Goosse 2003):

$$\dot{m}_{WDW} = \dot{m}_0 \gamma \frac{0.5°C - \Phi_{300m}}{-1.8°C - \Phi_{300m}}. \qquad (12)$$

Here, 0.5°C is a typical WDW temperature and −1.8°C is typical present-day ice shelf cavity temperature (Hattermann et al. 2012); Φ_{300m} is the melting point temperature at 300-m depth, which is approximately the mean depth of the ice shelf draft in the study region. While it is assumed that all available heat is used for melting under cold present-day conditions, the efficiency coefficient γ (Nøst et al. 2011) describes how much of the available heat contributes to basal melting, which appears to be the limiting factor when water that is significantly warmer than the surface freezing point enters the cavity (Little et al. 2009). A moderate value of $\gamma = 0.3$ is chosen for (12) accounting for the fact that other waters will enter the cavity besides the warmest WDW and—as will be shown shortly—assuring that physical meaningful steady-state solutions exist within the given forcing range. As a result, the area-averaged melt rates increase threefold from 0.4 m yr^{-1} (Rignot et al. 2013) to 1.2 m yr^{-1} when the thermocline rises above the shelf break.

The meltwater flux along the perimeter is then parameterized as a function of the local thermocline depth,

$$\dot{m}(h) = \begin{cases} \dot{m}_0, & \text{for} \quad z_{tcl} \geq 500\,\text{m} \\ \dot{m}_{WDW}, & \text{for} \quad z_{tcl} \leq 500\,\text{m} \end{cases}, \qquad (13)$$

with a transition depth of $z_{tcl} = 500$ m (for $D - H = 150$ m equivalent to $\Delta z_{tcl} = 350$ m), which corresponds to the approximate depth of the shelf break.

The dependence of the residual buoyancy flux on the thermocline depth in (11) introduces a nonlinearity to the model that yields multiple solutions depending on whether the thermocline is above or below the shelf break. Analog to (9), a steady-state solution for the thermocline depth can be derived using (11) in (1):

$$\Delta z_{tcl} = \sqrt{\frac{2L(\tau + B_{\dot{m}} f \rho_0 / \Delta\rho)}{cg\Delta\rho}}. \qquad (14)$$

Figure 11 shows solutions of (14) for different melt rates as a function of density forcing for climatological mean wind stress. Compared to the case without basal melting ($\Delta\rho = 0.25$ kg m^{-3}, $\Delta_{tcl} = 380$ m), the present-day
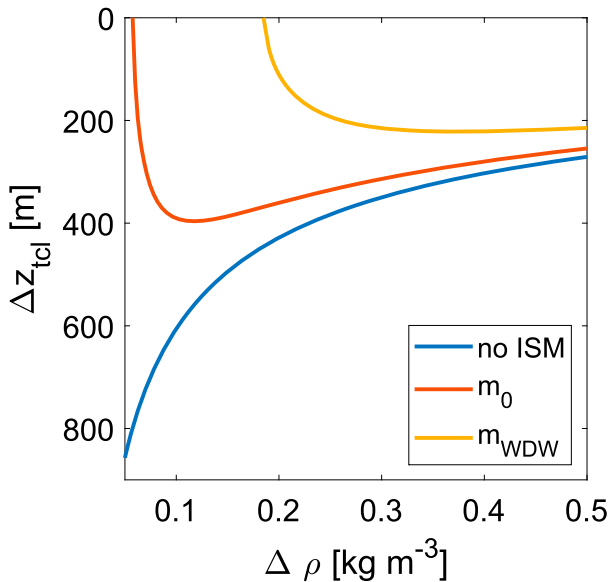
FIG. 11. Steady-state solutions of the thermocline depression depth for varying layer density difference and climatological mean wind forcing. The curve labeled m_0 uses present-day meltwater fluxes, and the curve labeled m_{WDW} uses meltwater fluxes from (12) in (14), showing the existence of multiple steady-state solutions when basal melting is included in the model.

meltwater flux m_0 yields a 50-m shallower thermocline for the climatological mean density difference. For the same forcing, a high melting state solution with a 190 m shallower thermocline exists ($\Delta_{tcl} = 190$ m). In this state, the corresponding net onshore WDW transport increases from about 0.2 Sv with present-day melt rates to 0.9 Sv to balance the increased buoyancy flux.

Without basal melting, the thermocline deepens asymptotically with decreasing density difference. When basal melting is added, a maximum thermocline depth is found where the response to changes in density forcing reverses. Figure 11 shows a steep rise of the thermocline for decreasing density until the numerator in (14) vanishes and no physical solution exists below a certain threshold. For higher melt rates, the reversal occurs at larger density differences, because meltwater fluxes dominate the dense water transport into the boundary current. As a consequence of the reversed regime, the system does not exhibit a closed hysteresis loop, in which the elevated thermocline state of high melting could be switched back into a state of low melting by decreasing the density difference. Instead the model suggests a collapse of the slope front with decreasing density difference once the thermocline resides above the shelf break.

f. Transient freshening projections

Researchers de Lavergne et al. (2014) found that the pycnocline strength of Antarctic surface waters has

increased by $4.5\,\mathrm{g\,m^{-3}\,decade^{-1}}$ over the past 60 years. Using this trend to compute changes in thermocline depression around the climatological mean wind stress and density difference from (9) yields a rise of the thermocline by $3.4\,\mathrm{m\,decade^{-1}}$. To illustrate the effect of the meltwater feedback in the context of the upper ocean freshening, three 150-yr-long transient runs were performed, where the observed freshening trend is added to the prescribed seasonal variability of the density difference forcing. The first run includes no ice shelf meltwater (ISM) fluxes (no ISM), the second run prescribes a constant present-day input $\dot{m}_0$ (constant ISM), and the third run employs a variable meltwater input (variable ISM) based on the local thermocline position according to (13). Time-varying eastern inflow conditions are equal in all runs and were obtained from the steady-state solution without meltwater fluxes [(9)] for the slowly increasing annual mean density difference, to reflect the large-scale adjustment to the applied freshening trend. Other than that, the model setup and forcing are equivalent to those in the wind and $\Delta\rho$ run in section 4d.

Figure 12a shows that the annual mean thermocline depth (averaged along the perimeter) continuously rises in all three runs as a consequence of the increasing density difference between the layers. Compared to the no ISM run, the constant melting lifts the thermocline by an offset that slightly decreases with time because of the reduced relative importance of the meltwater input for increasing density differences. However, when variable meltwater fluxes are included, the thermocline abruptly shifts to a higher mean position approximately 40 years into the simulation, when the seasonally varying thermocline position remains above the transition depth for the most part of the year.

Figure 12b shows the thermocline evolution along the model perimeter at different times during the variable ISM run. While the layer interface remains constant in alongslope direction in the no ISM solution (not shown), the thermocline rises by about 30 m along the boundary current as a consequence of the residual overturning caused by the meltwater input. The shift into the high melting state amplifies this trend, with differences in thermocline depth between year 1 and year 50 being approximately twice as large at the outflow boundary compared to the inflow position. An increased amplitude of the annual cycle during the period when the thermocline intermittently moves above the transition depth is also shown by the thin red curve in Fig. 12b, which corresponds to the seasonal thermocline anomaly at the model outflow boundary during the first year of the variable ISM run shown in Fig. 10.

A major challenge is to determine if and under which conditions such a regime shift could occur. The onshore heat transport in the Weddell Sea may respond to
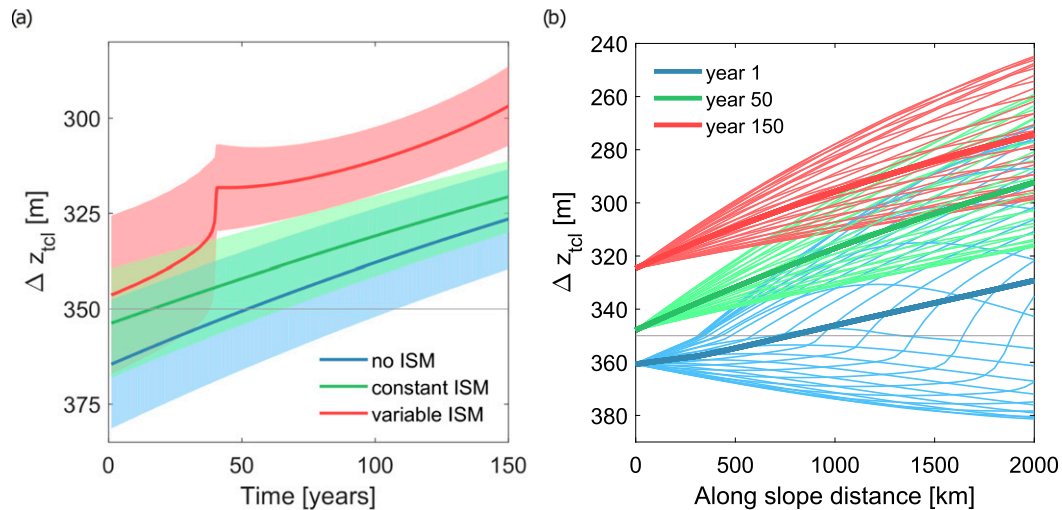
FIG. 12. (a) Time series of thermocline depression at the outflow model boundary for a transient increase in pycnocline strength by 4.5 g m^{-3} per decade. Solid curves show the annual mean; shaded areas indicate the seasonal variability of the respective model run. (b) Evolution of the thermocline depression along the model perimeter for three different time periods in the run with variable meltwater input. Thick solid curves show the annual mean; thin curves indicate the seasonal variability for each time slice.

relatively small depth changes of the thermocline which resides close to the shelf break. However, a more gradual transition between the low-state and high-state melting is expected than prescribed by the step function in (13), which appeared to be the simplest approach for obtaining the multiple steady-state solutions shown in Fig. 11. The response of the frontal overturning to meltwater fluxes will also depend on the applied eddy closure (Stewart and Thompson 2016) and the explicit evolution of the density field that is not included in the model. Nevertheless, the simple model shows that the response to increased ice shelf melting is of comparable magnitude to the effects of the observed freshening trend. It also illustrates the underlying mechanism of a possible tipping point through the ice shelf melting feedback, which is confirmed by sensitivity studies with an idealized general circulation model presented in appendix B.

5. Summary and conclusions

The combination of hydrographic observations from historic cruises with recently emerging data from animal platforms provided new insights on the spatial structure and seasonality of the Antarctic Slope Front (ASF) along the narrow continental shelf in the eastern Weddell Sea. The correspondence of the significant shoaling of the warm deep water (WDW) between November and May at Kapp Norvegia with warmer inflows onto the continental shelf near the Filchner Trough suggests a coherent seasonal evolution of the thermocline depth along a larger portion of the coast.

Although there is a general consensus that easterly winds are suppressing warm water along the shelf break around Antarctica, the seasonal imprint of the wind forcing is not evident at first sight from the data analysis in this study. The rise of the thermocline seems somewhat out of phase with the basinwide wind stress that increases over the same time period (Fig. 10). While local Ekman transport would adjust on shorter time scales, Su et al. (2014) suggested that a lag of several months may be inherent to the resonance of the seasonal wind forcing in a circular basin, whereas Nuñez-Riboni and Fahrbach (2009) argued that the seasonal presence of sea ice may alter the momentum transfer into the ocean on seasonal scales. The thermocline depth estimates derived from the hydrographic data remain too scattered in time and space to definitely discriminate between either of the above mechanisms. Instead, the climatological cross sections of the ASF show that the shoaling of the WDW is concurrent with a freshening at the shelf break, suggesting that seasonal upper ocean buoyancy fluxes are likely to be another driver of the observed variability. In this mechanism, downwelling of fresh and buoyant Antarctic Surface Water (ASW) increases potential energy at a secondary front above the thermocline. Enhanced baroclinic growth rates suggest that a shallow eddy overturning cell exists at the shelf break during summer, which partially compensates the wind driven deepening of the WDW.

The proposed role of the upper ocean buoyancy forcing for the frontal momentum balance is supported by Nuñez-Riboni and Fahrbach (2009), who argue that thermohaline forcing is a major contributor to the slope

current variability. They observed increased baroclinic currents at the prime meridian from January to April that match well with the appearance of the ASW in the hydrographic cross sections (Fig. 4). Direct measurements of cross frontal momentum balance between Ekman and eddy transports on seasonal scales are lacking, but Jensen et al. (2013) observed elevated eddy kinetic energy and wave activity at the shelf in summer and autumn that is consistent with increased instability of the current when ASW is present in the water column. While Semper and Darelius (2017) suggested that increased stratification enhances vertical mixing at the shelf break, numerical simulations confirm that upper ocean freshening yields a shallower thermocline (Hattermann et al. 2014) and increases the onshore eddy transport (Daae et al. 2017).

Other processes such as tides (Stewart et al. 2018), the interaction of the ASF undercurrent (Chavanne et al. 2010) with coastal troughs (St-Laurent et al. 2013), and local controls of the ice topography (Price et al. 2008; Langley et al. 2014) will modulate the response to the large-scale forcing. Transients such as distinct storm events (Darelius et al. 2016), lateral advection of hydrographic anomalies (Graham et al. 2013), or local surface buoyancy fluxes (Petty et al. 2013) are likely to dominate the thermocline depth variability on shorter time scales. However, these effects will superimpose onto the background state that is set by the time-integrated forcing, and typically remains close to the steady-state equilibrium on seasonal time scales and longer, which are the time scales investigated in this study.

An idealized model of the slope front overturning was formulated to predict the thermocline depth as a function of wind forcing and the density gradient across the front. Despite its simplicity, the model correctly scales the depression of the WDW and yields steady-state solutions [(9)] that are largely independent of model specific parameters. Transient simulations suggest that the respective response to changes in wind stress and upper-ocean density are of comparable magnitude and combine additively to produce the observed seasonal shoaling and deepening of the thermocline along the continental slope.

While responding approximately linearly to seasonal changes in wind forcing, the thermocline deepens asymptotically for smaller density differences, indicating that the densification of the surface water due to sea ice production in winter is important for maintaining the deep thermocline that separates the WDW from the ice shelves in the Weddell Sea. Today, upper ocean buoyancy fluxes along the narrow shelf region are largely determined by the interaction between sea ice formation and melting and surface Ekman transport (Nøst et al. 2011; Zhou et al. 2014). Increased precipitation and reduced sea ice formation (de Lavergne et al. 2014) might change this situation in a future climate, yielding a tipping point in which increased buoyancy fluxes from basal melting maintain a high thermocline state. The susceptibility for such a transition in the Weddell Sea is consistent with the predicted increase of melting in the eastern Weddell Sea (Kusahara and Hasumi 2013) and the rise of the thermocline that triggers the warm water inflow beneath the Filchner Ice Shelf in Hellmer et al. (2017). Increasing easterly winds may counteract this regime shift in the Weddell Sea that also depends strongly on the atmospheric forcing (Timmermann and Hellmer 2013), as well as on the details of the melting response and freshwater distribution above the thermocline that are not captured by the simple model in this study.

Being applicable to any narrow shelf region with easterly winds around Antarctica, the principal mechanism could also be representative for the warm shelves in parts of West Antarctica where an ASF is present (e.g., near the Dotson and Getz Ice Shelves at the western boundary of the Ross Gyre in the eastern Amundsen Sea), and meltwater fluxes are found to maintain the onshore heat transport (Jourdain et al. 2017). Dedicated observations of the slope front and shelf break thermocline depth are needed to better understand the role of upper ocean buoyancy fluxes on the frontal momentum balance. To predict the response of the onshore heat transport and basal melting in future climate, high-resolution numerical models are needed. Besides giving new insights into the slope front dynamics, the climatological hydrographic cross sections that were derived in this study (Hattermann and Rohardt 2018) can help to constrain and evaluate those models.

APPENDIX A

Wind-Driven Transport

The original (1) in Straneo (2006) for the interior thickness evolution is extended by introducing a spatially uniform wind-driven Ekman transport $\tau_s/\rho f$ that advects upper-layer properties into the boundary current and is exactly balanced by a return flow at the bottom.
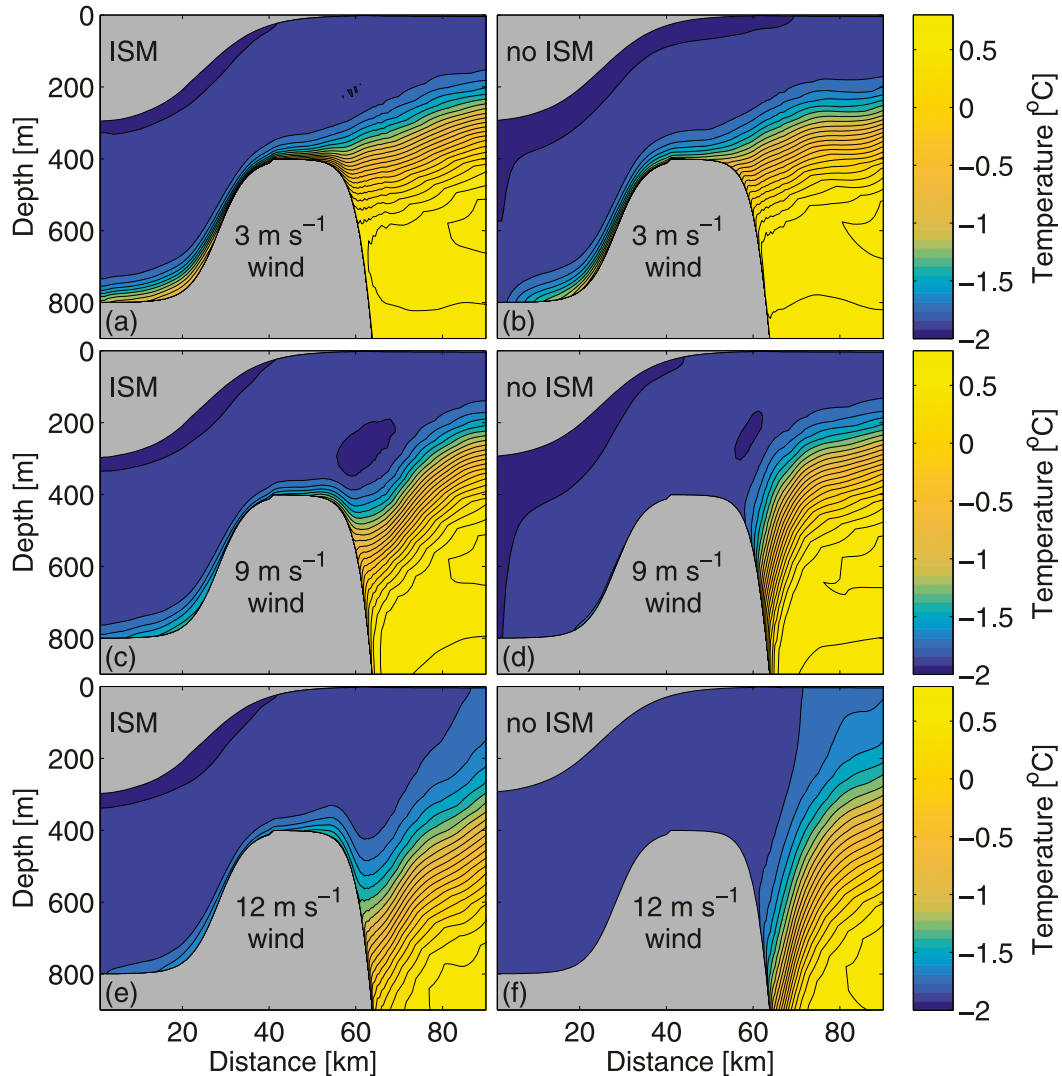
FIG. B1. Zonally averaged temperature fields from an idealized periodic channel model of the slope front overturning with different wind forcings, showing (left) day 180 of the experiments with ice shelf melting included, equivalent to Fig. 13 in Nøst et al. (2011), and (right) the same simulations without meltwater fluxes at the ice base.

Integrating the total transport along the perimeter and scaling with the basin surface A, this yields an additional source term for the interior thickness evolution:

$$\frac{dD}{dt}(V_e) = \frac{\tau_s}{\rho f}\frac{P}{2\pi R} = \frac{V_e}{A}. \qquad (A1)$$

For the boundary current, a similar source term is obtained from mass conservation for the layer thickness evolution integrated along the perimeter

$$\frac{d}{dt}\int h_2\,dl = -\frac{V_e}{L}, \qquad (A2)$$

which for a uniform wind stress simplifies to

$$\frac{\partial}{\partial l}\int\frac{\partial h_2}{\partial t}dl = -\frac{\partial}{\partial l}\frac{\tau_s}{\rho f}\frac{P}{L}, \quad \text{and} \qquad (A3)$$

$$\frac{\partial h_2}{\partial t}(V_e) = -\frac{V_e}{PL}. \qquad (A4)$$

APPENDIX B

Effects of Ice Shelf Melting on the Slope Front Overturning

Nøst et al. (2011) showed that eddies may transport denser and warmer water onto the continental shelf along the eastern Weddell Sea. To demonstrate the

effect of meltwater fluxes from adjacent ice shelves onto this frontal overturning, the numerical experiments with the idealized periodic channel model described in Nøst et al. (2011) are compared with simulations using the same setup, but without including the thermohaline forcing at the ice shelf base (Fig. B1). For weak wind forcing of $3\,\mathrm{m\,s}^{-1}$, a warm bottom layer in the ice shelf cavity exists in both cases, because of the relatively shallow thermocline. For stronger winds, however, the thermocline is depressed below the shelf break and the upward sloping isopycnals, which occur because eddies lift warm water over the sill to compensate the buoyancy forcing inside the ice shelf cavity, disappear when meltwater fluxes are turned off.

REFERENCES

Årthun, M., K. W. Nicholls, K. Makinson, M. A. Fedak, and L. Boehme, 2012: Seasonal inflow of warm water onto the southern Weddell Sea continental shelf, Antarctica. *Geophys. Res. Lett.*, **39**, L17601, https://doi.org/10.1029/2012GL052856.

Barker, P. M., and T. J. McDougall, 2017: Stabilizing hydrographic profiles with minimal change to the water masses. *J. Atmos. Oceanic Technol.*, **34**, 1935–1945, https://doi.org/10.1175/JTECH-D-16-0111.1.

Beckmann, A., and H. Goosse, 2003: A parameterization of ice shelf–ocean interaction for climate models. *Ocean Modell.*, **5**, 157–170, https://doi.org/10.1016/S1463-5003(02)00019-7.

Bernardello, R., I. Marinov, J. B. Palter, J. L. Sarmiento, E. D. Galbraith, and R. D. Slater, 2014: Response of the ocean natural carbon storage to projected twenty-first-century climate change. *J. Climate*, **27**, 2033–2053, https://doi.org/10.1175/JCLI-D-13-00343.1.

Boehme, L., P. Lovell, M. Biuw, F. Roquet, J. Nicholson, S. E. Thorpe, M. P. Meredith, and M. Fedak, 2009: Technical note: Animal-borne CTD-satellite relay data loggers for real-time oceanographic data collection. *Ocean Sci.*, **5**, 685–695, https://doi.org/10.5194/os-5-685-2009.

Chavanne, C. P., K. J. Heywood, K. W. Nicholls, and I. Fer, 2010: Observations of the Antarctic slope undercurrent in the southeastern Weddell Sea. *Geophys. Res. Lett.*, **37**, L13601, https://doi.org/10.1029/2010GL043603.

Couldrey, M. P., L. Jullion, A. C. Naveira Garabato, C. Rye, L. Herraiz-Borreguero, P. J. Brown, M. P. Meredith, and K. L. Speer, 2013: Remotely induced warming of Antarctic Bottom Water in the eastern Weddell gyre. *Geophys. Res. Lett.*, **40**, 2755–2760, https://doi.org/10.1002/grl.50526.

Daae, K., T. Hattermann, E. Darelius, and I. Fer, 2017: On the effect of topography and wind on warm water inflow—An idealized study of the southern Weddell Sea continental shelf system. *J. Geophys. Res. Oceans*, **122**, 2622–2641, https://doi.org/10.1002/2016JC012541.

Darelius, E., I. Fer, and K. W. Nicholls, 2016: Observed vulnerability of Filchner-Ronne Ice Shelf to wind-driven inflow of warm deep water. *Nat. Commun.*, **7**, 12300, https://doi.org/10.1038/ncomms12300.

de Lavergne, C., J. B. Palter, E. D. Galbraith, R. Bernardello, and I. Marinov, 2014: Cessation of deep convection in the open Southern Ocean under anthropogenic climate change. *Nat. Commun.*, **4**, 278–282, https://doi.org/10.1038/nclimate2132.

D'Errico, J. R., 2006: Surface fitting using gridfit. MathWorks, accessed 19 March 2018, https://mathworks.com/matlabcentral/fileexchange/8998-surface-fitting-using-gridfit.

Eady, E. T., 1949: Long waves and cyclone waves. *Tellus*, **1**, 33–52, https://doi.org/10.3402/tellusa.v1i3.8507.

Fahrbach, E., G. Rohardt, and G. Krause, 1992: The Antarctic Coastal Current in the southeastern Weddell Sea. *Polar Biol.*, **12**, 171–182, https://doi.org/10.1007/BF00238257.

——, ——, M. Schröder, and V. Strass, 1994: Transport and structure of the Weddell Gyre. *Ann. Geophys.*, **12**, 840–855, https://doi.org/10.1007/s00585-994-0840-7.

Fedak, M., 2004: Marine mammals as platforms for oceanographic sampling: A ''win/win'' situation for biology and operational oceanography. *Mem. Nat. Inst. Polar Res.*, **58**, 133–147.

Fraser, A. D., R. A. Massom, K. J. Michael, B. K. Galton-Fenzi, and J. L. Lieser, 2012: East Antarctic landfast sea ice distribution and variability, 2000–08. *J. Climate*, **25**, 1137–1156, https://doi.org/10.1175/JCLI-D-10-05032.1.

Fretwell, P., and Coauthors, 2013: Bedmap2: Improved ice bed, surface and thickness datasets for Antarctica. *Cryosphere*, **7**, 375–393, https://doi.org/10.5194/tc-7-375-2013.

Graham, J. A., K. J. Heywood, C. P. Chavanne, and P. R. Holland, 2013: Seasonal variability of water masses and transport on the Antarctic continental shelf and slope in the southeastern Weddell Sea. *J. Geophys. Res. Oceans*, **118**, 2201–2214, https://doi.org/10.1002/jgrc.20174.

Hattermann, T., and G. Rohardt, 2018: Kapp Norvegia Antarctic Slope Front climatology. Alfred Wegener Institute, Helmholtz Center for Polar and Marine Research, accessed 22 September 2018, https://doi.pangaea.de/10.1594/PANGAEA.893199.

——, O. A. Nøst, J. M. Lilly, and L. H. Smedsrud, 2012: Two years of oceanic observations below the Fimbul Ice Shelf, Antarctica. *Geophys. Res. Lett.*, **39**, L12605, https://doi.org/10.1029/2012GL051012.

——, L. Smedsrud, O. Nøst, J. Lilly, and B. Galton-Fenzi, 2014: Eddy-resolving simulations of the Fimbul Ice Shelf cavity circulation: Basal melting and exchange with open ocean. *Ocean Modell.*, **82**, 28–44, https://doi.org/10.1016/j.ocemod.2014.07.004.

Hellmer, H. H., F. Kauker, R. Timmermann, J. Determann, and J. Rae, 2012: Twenty-first-century warming of a large Antarctic ice-shelf cavity by a redirected coastal current. *Nature*, **485**, 225–228, https://doi.org/10.1038/nature11064.

——, ——, ——, and T. Hattermann, 2017: The fate of the southern Weddell Sea continental shelf in a warming climate. *J. Climate*, **30**, 4337–4350, https://doi.org/10.1175/JCLI-D-16-0420.1.

Heywood, K. J., R. A. Locarnini, R. D. Frew, P. F. Dennis, and B. A. King, 1998: Transport and water masses of the Antarctic Slope Front system in the eastern Weddell Sea. *Ocean, Ice and Atmosphere: Interactions at the Antarctic Continental Margin*, S. S. Jacobs and R. F. Weiss, Eds., Amer. Geophys. Union, 203–214.

——, A. C. Naveira Garabato, D. P. Stevens, and R. D. Muench, 2004: On the fate of the Antarctic Slope Front and the origin of the Weddell Front. *J. Geophys. Res.*, **109**, C06021, https://doi.org/10.1029/2003JC002053.

Hoppema, M., K. Bakker, S. M. van Heuven, J. C. van Ooijen, and H. J. de Baar, 2015: Distributions, trends and inter-annual variability of nutrients along a repeat section through the Weddell Sea (1996–2011). *Mar. Chem.*, **177**, 545–553, https://doi.org/10.1016/j.marchem.2015.08.007.

Isachsen, P. E., 2011: Baroclinic instability and eddy tracer transport across sloping bottom topography: How well does a modified Eady model do in primitive equation simulations?

Ocean Modell., **39**, 183–199, https://doi.org/10.1016/j.ocemod.2010.09.007.

Jensen, M. F., I. Fer, and E. Darelius, 2013: Low frequency variability on the continental slope of the southern Weddell Sea. *J. Geophys. Res. Oceans*, **118**, 4256–4272, https://doi.org/10.1002/jgrc.20309.

Jourdain, N. C., P. Mathiot, N. Merino, G. Durand, J. Le Sommer, P. Spence, P. Dutrieux, and G. Madec, 2017: Ocean circulation and sea-ice thinning induced by melting ice shelves in the Amundsen Sea. *J. Geophys. Res. Oceans*, **122**, 2550–2573, https://doi.org/10.1002/2016JC012509.

Jullion, L., and Coauthors, 2014: The contribution of the Weddell Gyre to the lower limb of the global overturning circulation. *J. Geophys. Res. Oceans*, **119**, 3357–3377, https://doi.org/10.1002/2013JC009725.

Kusahara, K., and H. Hasumi, 2013: Modeling Antarctic ice shelf responses to future climate changes and impacts on the ocean. *J. Geophys. Res. Oceans*, **118**, 2454–2475, https://doi.org/10.1002/jgrc.20166.

Laken, B., and J. Čalogović, 2013: Composite analysis with Monte Carlo methods: An example with cosmic rays and clouds. *J. Space Wea. Space Climate*, **3**, A29, https://doi.org/10.1051/swsc/2013051.

Langley, K., and Coauthors, 2014: Low melt rates with seasonal variability at the base of Fimbul Ice Shelf, East Antarctica, revealed by in situ interferometric radar measurements. *Geophys. Res. Lett.*, **41**, 8138–8146, https://doi.org/10.1002/2014GL061782.

Little, C. M., A. Gnanadesikan, and M. Oppenheimer, 2009: How ice shelf morphology controls basal melting. *J. Geophys. Res.*, **114**, C12007, https://doi.org/10.1029/2008JC005197.

Lüpkes, C., and G. Birnbaum, 2005: Surface drag in the Arctic marginal sea-ice zone: A comparison of different parameterisation concepts. *Bound.-Layer Meteor.*, **117**, 179–211, https://doi.org/10.1007/s10546-005-1445-8.

Marshall, J., and T. Radko, 2003: Residual-mean solutions for the Antarctic Circumpolar Current and its associated overturning circulation. *J. Phys. Oceanogr.*, **33**, 2341–2354, https://doi.org/10.1175/1520-0485(2003)033<2341:RSFTAC>2.0.CO;2.

Mensah, V., F. Roquet, L. Siegelman-Charbit, B. Picard, E. Pauthenet, and C. Guinet, 2018: A correction for the thermal mass–induced errors of CTD tags mounted on marine mammals. *J. Atmos. Oceanic Technol.*, **35**, 1237–1252, https://doi.org/10.1175/JTECH-D-17-0141.1.

Nakanowatari, T., and Coauthors, 2017: Hydrographic observations by instrumented marine mammals in the Sea of Okhotsk. *Polar Sci.*, **13**, 56–65, https://doi.org/10.1016/j.polar.2017.06.001.

Naughten, K. A., K. J. Meissner, B. K. Galton-Fenzi, M. H. England, R. Timmermann, and H. H. Hellmer, 2018: Future projections of Antarctic ice shelf melting based on CMIP5 scenarios. *J. Climate*, **31**, 5243–5261, https://doi.org/10.1175/JCLI-D-17-0854.1.

Naveira Garabato, A. C., and Coauthors, 2017: Vigorous lateral export of the meltwater outflow from beneath an Antarctic ice shelf. *Nature*, **542**, 219–222, https://doi.org/10.1038/nature20825.

Nicholls, K. W., S. Østerhus, K. Makinson, T. Gammelsrød, and E. Fahrbach, 2009: Ice-ocean processes over the continental shelf of the southern Weddell Sea, Antarctica: A review. *Rev. Geophys.*, **47**, RG3003, https://doi.org/10.1029/2007RG000250.

Nøst, O. A., and T. Lothe, 1997: The Antarctic Coastal Current—Physical oceanographic results from NARE 1996/97. *Norsk Polarinstitutt Meddelelser*, J. G. Winther, Ed., Vol. 148, Norsk Polarinstitutt, 51–57.

——, M. Biuw, V. Tverberg, C. Lydersen, T. Hattermann, Q. Zhou, L. H. Smedsrud, and K. M. Kovacs, 2011: Eddy overturning of the Antarctic Slope Front controls glacial melting in the eastern Weddell Sea. *J. Geophys. Res.*, **116**, C11014, https://doi.org/10.1029/2011JC006965.

Nuñez-Riboni, I., and E. Fahrbach, 2009: Seasonal variability of the Antarctic Coastal Current and its driving mechanisms in the Weddell Sea. *Deep-Sea Res. I*, **56**, 1927–1941, https://doi.org/10.1016/j.dsr.2009.06.005.

Ohshima, K. I., T. Takizawa, S. Ushio, and T. Kawamura, 1996: Seasonal variations of the Antarctic coastal ocean in the vicinity of Lützow-Holm Bay. *J. Geophys. Res.*, **101**, 20 617–20 628, https://doi.org/10.1029/96JC01752.

Orsi, A. H., W. M. Smethie, and J. L. Bullister, 2002: On the total input of Antarctic waters to the deep ocean: A preliminary estimate from chlorofluorocarbon measurements. *J. Geophys. Res.*, **107**, 3122, https://doi.org/10.1029/2001JC000976.

Parkinson, C. L., and D. J. Cavalieri, 2012: Antarctic sea ice variability and trends, 1979–2010. *Cryosphere*, **6**, 871–880, https://doi.org/10.5194/tc-6-871-2012.

Pellichero, V., J.-B. Salleé, S. Schmidtko, F. Roquet, and J.-B. Charrassin, 2017: The ocean mixed layer under Southern Ocean sea-ice: Seasonal cycle and forcing. *J. Geophys. Res. Oceans*, **122**, 1608–1633, https://doi.org/10.1002/2016JC011970.

Peña-Molino, B., M. S. McCartney, and S. R. Rintoul, 2016: Direct observations of the Antarctic Slope Current transport at 113°E. *J. Geophys. Res. Oceans*, **121**, 7390–7407, https://doi.org/10.1002/2015JC011594.

Petty, A. A., D. L. Feltham, and P. R. Holland, 2013: Impact of atmospheric forcing on Antarctic continental shelf water masses. *J. Phys. Oceanogr.*, **43**, 920–940, https://doi.org/10.1175/JPO-D-12-0172.1.

Price, M. R., K. J. Heywood, and K. W. Nicholls, 2008: Ice-shelf–ocean interactions at Fimbul Ice Shelf, Antarctica from oxygen isotope ratio measurements. *Ocean Sci.*, **4**, 89–98, https://doi.org/10.5194/os-4-89-2008.

Pritchard, H. D., S. R. M. Ligtenberg, H. A. Fricker, D. G. Vaughan, M. R. van den Broeke, and L. Padman, 2012: Antarctic ice-sheet loss driven by basal melting of ice shelves. *Nature*, **484**, 502–505, https://doi.org/10.1038/nature10968.

Rignot, E., S. Jacobs, J. Mouginot, and B. Scheuchl, 2013: Ice-shelf melting around Antarctica. *Science*, **341**, 266–270, https://doi.org/10.1126/science.1235798.

Roquet, F., and Coauthors, 2014: A Southern Indian Ocean database of hydrographic profiles obtained with instrumented elephant seals. *Sci. Data*, **1**, 140028, https://doi.org/10.1038/sdata.2014.28.

Ryan, S., M. Schröder, O. Huhn, and R. Timmermann, 2016: On the warm inflow at the eastern boundary of the Weddell Gyre. *Deep-Sea Res.*, **107**, 70–81, https://doi.org/10.1016/j.dsr.2015.11.002.

——, T. Hattermann, E. Darelius, and M. Schröder, 2017: Seasonal cycle of hydrography on the eastern shelf of the Filchner Trough, Weddell Sea, Antarctica. *J. Geophys. Res. Oceans*, **122**, 6437–6453, https://doi.org/10.1002/2017JC012916.

Salleé, J.-B., E. Shuckburgh, N. Bruneau, A. J. S. Meijers, T. J. Bracegirdle, and Z. Wang, 2013: Assessment of Southern Ocean mixed-layer depths in CMIP5 models: Historical bias and forcing response. *J. Geophys. Res. Oceans*, **118**, 1845–1862, https://doi.org/10.1002/jgrc.20157.

Semper, S., and E. Darelius, 2017: Seasonal resonance of diurnal coastal trapped waves in the southern Weddell Sea, Antarctica. *Ocean Sci.*, **13**, 77–93, https://doi.org/10.5194/os-13-77-2017.

Smedsrud, L. H., 2005: Warming of the deep water in the Weddell Sea along the Greenwich meridian: 1977–2001. *Deep-Sea Res. I*, **52**, 241–258, https://doi.org/10.1016/j.dsr.2004.10.004.

Smith, K. S., 2007: The geography of linear baroclinic instability in Earth's oceans. *J. Mar. Res.*, **65**, 655–683, https://doi.org/10.1357/002224007783649484.

Spall, M. A., 2004: Boundary currents and water mass transformation in marginal seas. *J. Phys. Oceanogr.*, **34**, 1197–1213, https://doi.org/10.1175/1520-0485(2004)034<1197:BCAWTI>2.0.CO;2.

——, and D. C. Chapman, 1998: On the efficiency of baroclinic eddy heat transport across narrow fronts. *J. Phys. Oceanogr.*, **28**, 2275–2287, https://doi.org/10.1175/1520-0485(1998)028<2275:OTEOBE>2.0.CO;2.

Stewart, A. L., and A. F. Thompson, 2015: Eddy-mediated transport of warm Circumpolar Deep Water across the Antarctic Shelf Break. *Geophys. Res. Lett.*, **42**, 432–440, https://doi.org/10.1002/2014GL062281.

——, and ——, 2016: Eddy generation and jet formation via dense water outflows across the Antarctic Continental Slope. *J. Phys. Oceanogr.*, **46**, 3729–3750, https://doi.org/10.1175/JPO-D-16-0145.1.

——, A. Klocker, and D. Menemenlis, 2018: Circum-Antarctic shoreward heat transport derived from an eddy- and tide-resolving simulation. *Geophys. Res. Lett.*, **45**, 834–845, https://doi.org/10.1002/2017GL075677.

St-Laurent, P., J. M. Klinck, and M. S. Dinniman, 2013: On the role of coastal troughs in the circulation of warm Circumpolar Deep Water on Antarctic ice shelves. *J. Phys. Oceanogr.*, **43**, 51–64, https://doi.org/10.1175/JPO-D-11-0237.1.

Straneo, F., 2006: On the connection between dense water formation, overturning, and poleward heat transport in a convective basin. *J. Phys. Oceanogr.*, **36**, 1822–1840, https://doi.org/10.1175/JPO2932.1.

Su, Z., A. L. Stewart, and A. F. Thompson, 2014: An idealized model of Weddell Gyre export variability. *J. Phys. Oceanogr.*, **44**, 1671–1688, https://doi.org/10.1175/JPO-D-13-0263.1.

Sverdrup, H. U., 1953: The currents off the coast of Queen Maud Land. *Nor. Geogr. Tidsskr.*, **14**, 239–249, https://doi.org/10.1080/00291955308542731.

Teigen, S. H., F. Nilsen, R. Skogseth, B. Gjevik, and A. Beszczynska-Möller, 2011: Baroclinic instability in the West Spitsbergen Current. *J. Geophys. Res.*, **116**, C07012, https://doi.org/10.1029/2011JC006974.

Thompson, A. F., K. J. Heywood, S. Schmidtko, and A. L. Stewart, 2014: Eddy transport as a key component of the Antarctic overturning circulation. *Nat. Geosci.*, **7**, 879–884, https://doi.org/10.1038/ngeo2289.

Thompson, D. W. J., and S. Solomon, 2002: Interpretation of recent Southern Hemisphere climate change. *Science*, **296**, 895–899, https://doi.org/10.1126/science.1069270.

Timmermann, R., and H. H. Hellmer, 2013: Southern Ocean warming and increased ice shelf basal melting in the twenty-first and twenty-second centuries based on coupled ice-ocean finite-element modelling. *Ocean Modell.*, **63**, 1011–1026, https://doi.org/10.1007/s10236-013-0642-0.

——, and S. Goeller, 2017: Response to Filchner–Ronne Ice Shelf cavity warming in a coupled ocean–ice sheet model—Part 1: The ocean perspective. *Ocean Sci.*, **13**, 765–776, https://doi.org/10.5194/os-13-765-2017.

Treasure, A., and Coauthors, 2017: Marine mammals exploring the oceans pole to pole: A review of the MEOP consortium. *Oceanography*, **30**, 132–138, https://doi.org/10.5670/oceanog.2017.234.

Zhou, Q., T. Hattermann, O. A. Nøst, M. Biuw, K. M. Kovacs, and C. Lydersen, 2014: Wind-driven spreading of freshwater beneath the ice shelves in the Eastern Weddell Sea. *J. Geophys. Res. Oceans*, **119**, 3818–3833, https://doi.org/10.1002/2013JC009556.